ORNL/TM-2022/2572

Multi-Port Autonomous Reconfigurable Solar Power Plant

Suman Debnath
Phani Ratna
Vanamali Marthi
Qianxue Xia
Zerui Dong
Jiuping Pan
Shiyuan Yin
et al.

November 2022

OAK RIDGE National Laboratory

ORNL IS MANAGED BY UT-BATTELLE LLC FOR THE US DEPARTMENT OF ENERGY

ORNL/TM-2022/2572

DOE/EERE/Solar Energy Technology Office

MULTI-PORT AUTONOMOUS RECONFIGURABLE SOLAR POWER PLANT

Suman Debnath[1]
Phani Ratna Vanamali Marthi[1]
Qianxue Xia[1,2]
Zerui Dong[3]
Jiuping Pan[4]
Shiyuan Yin[2]
Hyo Jong Lee[4]
Rafal Wojda[1]
Anil Kondabathini[4]
Sudipta Chakraborty[3]
Maryam Saeedifard[2]
Reynaldo Nuqui[4]
Md Arifujjaman[5]

February 2023

Prepared by
OAK RIDGE NATIONAL LABORATORY
Oak Ridge, TN 37831
managed by
UT-BATTELLE LLC
for the
US DEPARTMENT OF ENERGY
under contract DE-AC05-00OR22725

[1] Oak Ridge National Laboratory
[2] Georgia Institute of Technology
[3] Opal-RT Corporation
[4] ABB/Hitachi Energy
[5] Southern California Edison

CONTENTS

LIST OF FIGURES

LIST OF TABLES

ABBREVIATED TERMS

ac	alternating current
AI	artificial intelligence
cHIL	control hardware-in-the-loop
CMD	command
CPU	central processing unit
D-MARS	Distribution Grid–Connected MARS
dc	direct current
DSP	digital signal processor
EBC	energy-balancing controller
EMS	energy management system
EMT	electromagnetic transient
ESS	energy storage system
FDI	false data injection
FDIA	false data injection attack
FPGA	field-programmable gate array
FPR	frequency-power response
G/NG	go/no-go
HIL	hardware-in-the-loop
HPC	high-performance computing
HVdc	high-voltage direct current
I/O	input/output
LCC	line-commuted converter
LCOE	levelized cost of electricity
LMP	locational marginal pricing
MARS	multi-port autonomous reconfigurable solar
MMC	modular multilevel converter
MOSFET	metal–oxide–semiconductor field-effect transistor
MPC	model-predictive control
MTdc	multiterminal DC
MVdc	medium-voltage DC
NARX	nonlinear autoregressive network with exogenous inputs

NERC	North American Electric Reliability Corporation
O&M	operation and maintenance
PCIe	peripheral component interconnection express
PE	power electronics
PI	proportional integral
PLL	phase-locked loop
PQ	active-reactive powers
PSCAD	power system computer aided design
PV	root-mean square
RMS	root-mean-square
ROCOF	rate of change of frequency
SCR	short-circuit ratio
SFP	small form-factor pluggable
SG	synchronous generator
SM	submodule
SNN	spiking neural network
SOC	state of charge
SVC	static var compensators
TDD	total demand distortion
VSC	voltage source converter
VSG	virtual synchronous generator
WECC	Western Electric Coordinating Council

ACKNOWLEDGMENTS

The project team included members from Oak Ridge National Laboratory, ABB, Hitachi Energy, Opal-RT Corporation, Georgia Institute of Technology, and Southern California Edison.

This material is based upon work supported by the U.S. Department of Energy's Office of Energy Efficiency and Renewable Energy (EERE) under the Advanced Power Electronics Design for Solar Applications FOA Award Number 34019.

The authors would like to acknowledge the support and feedback from John Seuss (U.S. DOE Solar Energy Technologies Office [SETO]) and Jian Fu (U.S. DOE Wind Energy Technologies Office [WETO]).

The authors would like to also thank the participants of the industry advisory board (IAB): Kevin Damron (Avista Corp), Kevin Chamberlain (Commonwealth Edison), Andrew Rockhill (Eaton), Siddharth Pant (General Electric), Timothy Lundeen (Jacksonville Electric Authority), James Okullo (Midcontinent Independent System Operator [MISO]), Jordan Bakke (MISO), Warren Hess (MISO), Andrew Arana (NextEra Energy), Jeffrey Plew (NextEra Energy), Nihal Mohan (NextEra Energy), Austin White (Oklahoma Gas & Electric [OGE]), Kandace Smith (OGE), Ryan Jones (OGE), Chenrui Jin (Pacific Gas & Electric [PGE]), Yu Zhang (PGE), Normann Fischer (Schweitzer Engineering Laboratories Inc.), Sergey Kynev (Siemens Energy), Andrew Ingram (Southern Company), Jonathan Glidewell (Southern Company), Casey Cathey (Southwest Power Pool [SPP]), Harvey Scribner (SPP), Madhav Manjrekar (University of North Carolina at Charlotte), Roy McCann (University of Arkansas), Eric Baran (Western Energy Board).

EXECUTIVE SUMMARY

As the penetration level of power electronics increases and remote photovoltaic (PV) generation is integrated into the alternating current (ac) grid, the short-circuit ratio (SCR) at the point of interconnection of a hybrid PV–energy storage system (ESS) plant may be low. Additionally, the inertia of the alternating current (ac) grid may be low. The low SCRs and inertias can lead to reliability challenges in the power grid. These operating conditions require additional reinforcements, such as synchronous condensers, static var compensators, static synchronous compensators, and high-voltage direct current (HVdc) links/grids. HVdc links or grids may also provide the additional capability of connecting the plant to asynchronous grids and/or connecting asynchronous grids, among others. This scenario leads to discrete development of solar inverters, energy storage inverters, HVdc converters, and several transformers. Some of the problems associated with this discrete development and inverter-based generation include increased cost, lower reliability, and reduced efficiency associated with duplication of power electronics (PEs); competing controls of several individual discrete inverter-based generators due to the presence of multiple PEs, which leads to derating of the system; and transient stability problems arising from inverter-based generation, such as voltage/frequency events leading inverter shutdowns, voltage instability and control interactions in the formed weak grid, and harmonics caused by resonances of multiple inverters.

The multi-port autonomous reconfigurable solar (MARS) power plant provides an economic integrated solution to connect PVs and ESSs directly to HVdc links or grids and ac transmission grids. It provides continuity of operation under low SCR conditions and both inertial and primary frequency response (also termed as fast frequency support) when a loss of generation happens. It also provides harmonized control of different resources (e.g., PV and ESS) within the plant and thus reduces competing controls and transient stability challenges.

In this project, the power electronics circuit configuration and hierarchical control system required in MARS is being investigated to integrate PV and ESS to HVdc and transmission ac grids. The concept is similar to the development of integrated circuits (when compared with discrete circuits) in computing. The circuit configuration is modular for ease of scalability in voltage and power ratings and for ease of integration of new PV and ESS modules. Methods to detect the injection of bad data or falsified data are incorporated into the MARS system. The methods, which are based on physics and artificial intelligence, detect infeasible commands or erroneous measurements sent to the hierarchical control system of MARS. The proposed MARS power electronics circuit and hierarchical control system, along with the intrusion detection algorithms, are evaluated in a hardware-in-the-loop configuration to quantify the technical benefits provided, such as up to 16% improvement in frequency response, 100% disturbance rejection, and 100% detection of intrusions under tests performed. Analysis has also shown the capability to reliably connect MARS to very low SCR regions. Two modules to integrate PV and ESS in MARS were developed in hardware to characterize the efficiency and cost of individual modules present in MARS. The efficiency and cost characterizations of individual modules in MARS have been used to quantify efficiency and electrical cost of MARS. Based on the cost assessments, up to 40% reduction in electrical costs and up to 25% reduction in levelized costs are anticipated in MARS as compared to discrete development in the baseline case. The discrete development results were obtained through separate development of PV, ESS, and HVdc systems. The reduction in quantified power losses is up to 50%.

Electricity generated from solar resources is expected to play an important role in meeting the recent clean energy target of 100% carbon pollution-free electricity by 2035. With solar resources dominant in the southern part as well as several remote regions of United States, there is value in transferring power through HVdc lines. Moreover, to transfer solar energy across asynchronous interconnections to load centers may also benefit from HVdc lines. There is also value to linking wind-rich regions with solar-rich

regions; exploiting the diversity of those resources can help with grid firming. This may also be achieved through the controllable HVdc lines. Additionally, energy storage is a dominant requirement that has been identified in the power grid to support the clean energy targets, most recently, through the launch of the Long-Duration Storage Shot as part of the US Department of Energy Earthshots Initiative.[6] These trends indicate the value of having an integrated solution that can connect solar and energy storage resources directly to HVdc lines and ac transmission grids. The MARS power plant is an important technology that can help meet clean energy targets by transferring solar power to remote load centers, provide an upgrade option to existing HVdc lines that are either underutilized and/or transferring coal power, and support links to multiterminal dc systems. MARS-type terminals will be located in remote regions that are rich in solar resources and thus are expected to support well-paid jobs in economically depressed and rural communities.

[6] https://www.energy.gov/eere/long-duration-storage-shot (accessed September 12, 2022).

1. INTRODUCTION

1.1 MARS CIRCUIT ARCHITECTURE

The multi-port autonomous reconfigurable solar (MARS) power plant enables connectivity of photovoltaics (PVs) and energy storage systems (ESSs) to high-voltage direct current (HVdc) links and transmission grids. It is modular and can autonomously reconfigure based on available energy. For example, in the absence of PV generation, MARS can continue to connect to the alternating current (ac) and direct current (dc) systems and provide energy from or to ESSs. The absence of PV generation may happen at nights and when there are faults within PV modules in MARS. Similarly, there are several other use cases where the autonomous reconfigurability to specific operation of MARS may happen. Some of the use cases include the following:

- MARS connects to ac/dc systems only;
- MARS connects PVs to ac/dc systems only;
- MARS connects ESSs to ac/dc systems only while charging ESSs;
- MARS connects ESSs to ac/dc systems only while discharging ESSs;
- MARS connects PVs and ESSs to ac/dc systems while charging ESSs; or
- MARS connects PVs and ESSs to ac/dc systems while discharging ESSs.

The need to connect combined PVs and ESSs to HVdc and transmission ac systems was not considered in prior research [1–19]. The concepts proposed in some research were evaluated in low-voltage or medium-voltage applications [1–4, 10–19]. Many of those concepts considered only PV or only ESS [1–2, 5–8, 11–13, 15–19]. In contrast, the MARS circuit configuration, proposed in this project, connects PVs and ESSs to HVdc and transmission ac grids.

1.2 SIMULATION ALGORITHMS

The MARS circuit configuration is novel and different from the circuit configurations of PV and ESS integrated modular multilevel converter (MMC) systems proposed in previous research endeavors [1–19]. The major difference between MARS and other proposed MMC-based configurations arises from the arrangement and integration of PV systems and ESSs to HVdc and transmission ac grid. In MARS, PV systems and ESSs are integrated directly with submodules (SMs) through dc-dc converters. This results in an increase in the number of states in the MARS system. In addition to states such as SM semiconductor states (insulated gate bipolar transistors, diodes), SM capacitor voltages, and arm inductor currents, the states from dc-dc converters (PV and ESS dc-dc converter semiconductor switching states, PV and ESS input capacitor voltages, and PV and ESS inductor currents) make the simulation time very long. Also, numerical stiffness identified in MARS adds to the computational complexity, and that results in long simulation time. These differences and issues call for a unique simulation algorithm to simulate the MARS system. Therefore, it is important to model and simulate MARS with an algorithm to reduce the imposed computational burdens. It may also be noted from prior art that a likely limiting factor to evaluate a large-scale PV-ESS system connecting to HVdc and transmission ac grids may have been related to the difficulty with developing models based on existing components in the library of the electromagnetic transient (EMT) simulator tool.

1.3 CONTROL ALGORITHMS & MARS CONTROL ARCHITECTURE

The MARS system can provide inertial and primary frequency response support and reject disturbances that were not considered in the prior research [1–19]. These improvements will enable continued operation under grid disturbances and reduced transient instability. The MARS system also incorporates an energy-balancing control to manage the PV, ESS, and HVdc systems for enhanced stability and coordination of resources. It also incorporates control methods to balance individual PV and ESS resources. To the best of the authors' knowledge, neither the detailed hierarchical control architecture of MARS, nor the control algorithms necessary to integrate PVs and ESSs to HVdc links and transmission ac grids has been evaluated in prior research.

1.4 ENERGY STORAGE SIZING

In the literature, several optimal sizing algorithms for ESSs in integrated PV and ESS (PV+ESS) power plants have been reported [20], [21]. In [20], the authors examine the operation of a large-scale PV system to achieve base-load generation. However, the economics associated with this approach is not studied. An energy management system (EMS) that enhances a medium sized PV farm's capability to produce constant power output and support peak load is designed in [21]. A comparison between two types of batteries (in ESSs), the lead-acid and the lithium-ion batteries, is also made in [21]; simulation results show that t the lead-acid batteries can make less annual revenue than the lithium-ion batteries and as a result, the lithium-ion battery is selected to demonstrate the proposed ESS sizing method. The optimization algorithms in [22]–[26] target residential and commercial buildings with rooftop PVs, and the corresponding algorithms cannot be applied to large-scale PV plants. The EMS proposed in [27] aims at enabling constant power generation during certain defined hours from the power plant. The power generated during the defined hours is optimized based on minimization of the battery state of charge (SOC) variations. However, the size of ESS is not obtained from an optimization algorithm. The number of days that the PV+ESS power plant cannot track the power output reference generated from the SOC optimization considering different ESS capacity is evaluated and used to determine the size of the ESS. This algorithm suffers from substantial computational burden. Moreover, it does not consider the economic aspect to determine the size of ESSs.

2. PROJECT OBJECTIVES

To meet the recent clean energy target of 100% carbon pollution–free electricity by 2035, electricity generated from solar resources is expected to play an important role. With solar resources dominant in the southern part as well as several remote regions of United States, there is value to transferring power through HVdc lines. Moreover, to transfer solar energy across asynchronous interconnections to load centers may also benefit from HVdc lines. Also, linking wind-rich regions with solar-rich regions to exploit the diversity of these resources can help with grid firming. This may also be achieved through the controllable HVdc lines. Additionally, energy storage is a dominant requirement that has been identified in the power grid to support the clean energy targets, most recently, through the launch of the long duration storage Earthshot. These trends indicate the value of having an integrated solution that can connect solar and energy storage resources directly to HVdc lines and transmission ac grids. MARS is an important technology that can help meet the clean energy targets set by transferring solar power to remote load centers, provide an upgrade option to existing HVdc lines that are either underutilized and/or transferring coal power, and support links to multi-terminal dc (MTdc). As MARS-type terminals will be locating in remote regions that rich in solar resources, it is expected to support well-paid jobs in several economically depressed and rural communities.

The tasks are summarized in Table 1 with milestones and go/no-go (G/NG) decision points. All milestones, tasks, and G/NG decision points were successfully completed.

Table 1. MARS tasks, milestones, and go/no-go decision points.

Task number	Task	Milestones
1	Define system and develop lumped ac models	M1.2 Identify requirements in MARS based on chosen site of interest and inputs from utilities. The requirements included ESS size in MW/MWh, PV size in MW, and dc capacity in MW/kV. M1.3 Develop ac dynamic models with at least 30 buses.
2	Design and develop reduced-order model of MARS	M2.0 Design and develop reduced-order model of MARS.
3	Develop simulation algorithms and high-fidelity models of MARS	M3.2 The preliminary developed simulation algorithm enables fast simulation. M3.4 Develop simulation algorithms and high-fidelity models for MARS. (G/NG)
4	Design and develop offline control algorithms in MARS	M4.2 Preliminary results from developed control algorithms in MARS. M4.5 Design and develop control algorithms in MARS. Preliminary business model presented. (G/NG)
5	Model cyber vulnerabilities and design cyber protection	M5.0 Develop two test cases for MARS vulnerability assessment.
6	Design PE module	M6.0 Design PE module. (G/NG)
7	Design control and HIL platforms	M7.0 Design HIL and control platforms. (G/NG)
8	Develop HIL and control platforms	M8.0 Develop HIL and control platforms.
9	Implement real-time PE-HIL algorithms	M9.0 Implement real-time PE-HIL algorithms.
10	Implement control algorithms in platform and validate	M10.0 Implement control algorithms in platform and evaluated. Updated business model presented.
11	Design and develop cyber hardware in lower-level controllers and implement cyber-secure solutions in higher-level controller	M11.0 Develop cyber hardware in lower-level controllers and implemented cyber-secure solutions in higher-level controller. (G/NG)
12	Develop PE module	M12.0 Develop PE module. (G/NG)
13	Develop ac system models in real-time system	M13.0 Develop ac system models in real-time system.
14	Implement cyber security algorithms and evaluate in MARS	M14.0 Implement cyber-security algorithms in MARS and evaluate.
15	Complete MARS system integration and evaluate performance	M15.2 Integrate PE-HIL with ac system real-time simulation and tested. M15.3 Integrate control system into MARS & test under various operating conditions. M15.4 Integrate cyber-security system and test under operating conditions. M15.5 Evaluate performance of the completely integrated MARS system.
16	Identify value proposition and develop business model for commercialization based on performance metrics, and HIL demonstration	M16.0 Develop business model for commercialization based on performance metrics.
17	Standards compliance of MARS	M17.0 Standards compliance tests for MARS

3. PROJECT RESULTS AND DISCUSSION

3.1 DEFINE SYSTEM AND DEVELOP LUMPED AC MODELS

3.1.1 Identify System Specifications

The locations where MARS can be integrated to the power grid were identified in California based on the location of large load centers [28–34], regions with high solar resources [35], and commissioned or potential HVdc lines [36–42]. Based on this information, two of the locations that were identified include Victorville in southern California, and Pittsburg in northern California (close to SFO), as shown in Figure 1. They are not the only sites in United States where MARS will be of interest; they are the sites chosen for this study to evaluate techno-economic benefits of MARS technology.

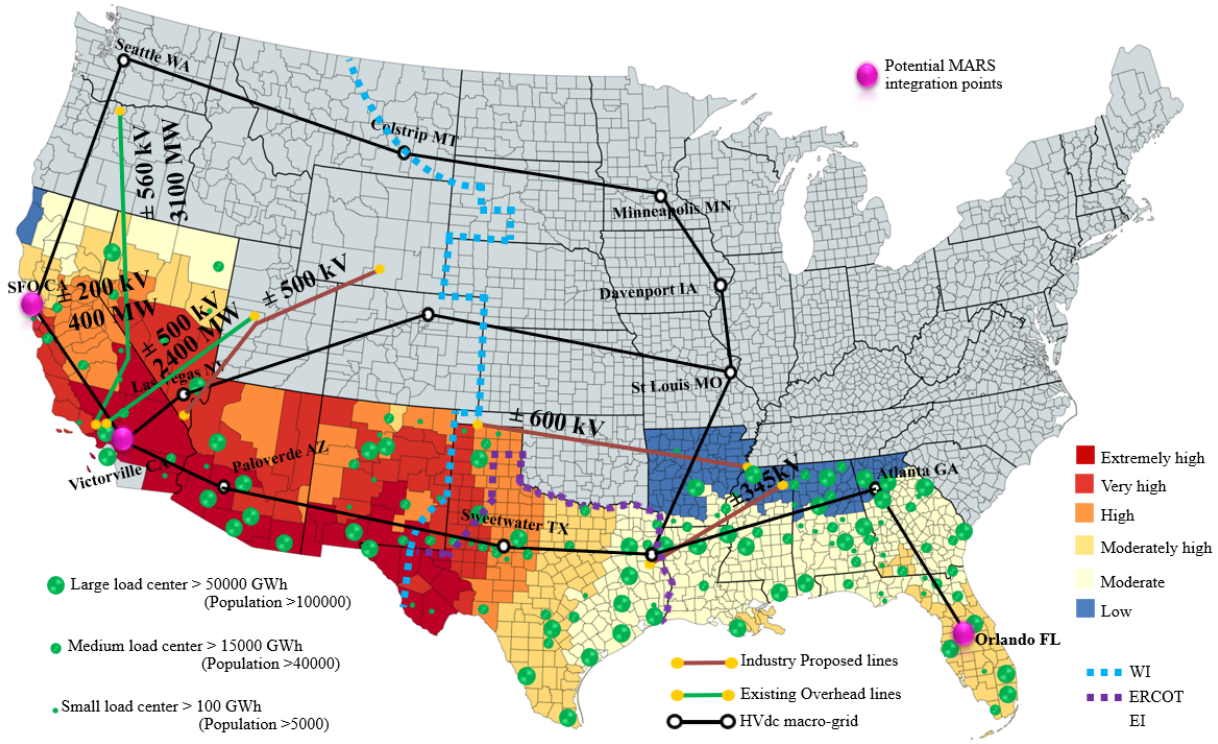

Figure 1. Options for the MARS integration system.

3.1.2 Identify ESS in Megawatts/Megawatt-Hours, PV Plant In Megawatts, and dc Capacity Requirements

The size of the PV system in MARS is based on the power transfer capability of the dc and ac lines in the region. The energy storage system for a PV power plant larger than 100 MW can be designed based on the assumption that the PV system acts as a base-load generation during the day. The power generated by PV system (P_{PV}) is estimated from PVWATTS [43]. Daytime base-load power generated from MARS (P_{MARS}) is calculated based on average power available from PV system in the 12 h window. The power required from energy storage (P_{ESS}) is calculated as

$$P_{\mathrm{ESS}} = -P_{\mathrm{PV}} + P_{\mathrm{MARS}} \tag{1}$$

System rating for two options is explored with the input parameters: fixed-array type with open rack and two-axis tracking.

Based on the aforementioned descriptions, the ratings of the MARS system with fixed-array type with open rack option for both locations are tabulated in Table 2. The size of energy storage is consistent with ESS sizing expected of the order of 4 h [44]. The numbers are similar with an optimization algorithm to size energy storage.

Table 2. Ratings for MARS integration at three potential locations with fixed-array photovoltaics.

Location	Pittsburg, California	Victorville, California
System rating (MW)	400.0	1000.0
dc voltage rating (kV)	±200.0	±525.0
ac voltage rating (kV)	220.0	500.0
PV rating (MW)	100.0	1000.0
ESS rating (MW)	32.8	389.8
ESS rating (MWh)	108.1	1,232.3

3.1.2.1 Advanced ESS sizing

In addition to the 12 h base-load generation design-based sizing of energy storage in MARS, a novel optimal sizing algorithm of a transmission grid-connected hybrid PV-ESS system is used to size the energy storage by maximizing the economics of operation. The objective function includes annual revenue generated from MARS based on locational marginal pricing (LMP) information available at the location, cost of energy storage, and benefits accrued from peak power generation. The constraints include power generated from PVs and ESSs and dispatched to the grid, state-of-charge (SOC) limits of energy storage, and energy stored in ESSs being equal at the end of each season. The algorithm performs a time-series simulation using 1-year data and maximizes the annual revenue by optimizing the ESS energy capacity. This problem is reduced to a 2-to-4-day problem with four to six changes assumed in power generation from hybrid PV-ESS based on pattern recognition in PV power available and the LMP value at the location. The optimal sizes of ESSs for different generation patterns at Pittsburg are given in Table 3. The 5LCPS1, which uses five changes in power generation, is within the range of ESS size given by the calculation of 12 h base-load generation design-based sizing of ESS and is the optimum configuration for Pittsburg. The optimization considers the 2-day results as well as the 1-year results in the table.

Table 3. Optimal sizing of ESSs in MARS at Pittsburg

Two-day power pattern configurations	Two-day optimum size of ESS (kWh)	One-year power pattern configurations	One-year ESS size (kWh)
5LCPS1	90,625.7	HCPS1	110,000
5LCPS2 (different time interval)	91,701.2	HCPS2	91,700

Milestone M 1.2, “Identify requirements in MARS based on chosen site of interest and inputs from utilities. The requirements will include ESS size in MW/MWh, PV size in MW, and dc capacity in MW/kV,” has been completed.

3.1.3 Identify Dynamic Models for at least One Study ac Transmission System Based on Utility Inputs

The contingencies to evaluate the performance of MARS' control systems are based on events that vary the frequency and voltage. To adequately represent the frequency behavior of a grid, a lumped representative dynamic model of the grid was developed based on the data-driven model developed in earlier research [45, 46]. The voltage behavior of the grid is a local phenomenon and was represented by the EMT models of the components close to the location of integrating MARS. The E-Tran tool has been utilized to convert the utility models of the local areas (Pittsburg and Victorville in California) from the "2025 Heavy Summer 1" Western Electric Coordinating Council (WECC) model in PSS®E into PSCAD EMT model. The converted local area EMT dynamic model in power system computer aided design (PSCAD) consists of the models of actual components in the local area, namely, Pittsburg and Victorville in California. It also consists of equivalent circuit models representing the dynamics of the rest of the WECC grid.

The equivalent circuit models include ac stiff voltage sources with internal impedances. The voltages at the terminals of these sources are defined along with the initial active and reactive powers. The frequency behavior of all the sources in the equivalent circuit model needs to be varied while the lumped dynamic model is being integrated into the local area dynamic model. This requires converting the ac stiff voltage sources with internal impedances and the voltages defined at the terminals into the controllable voltage sources with externally defined impedances. The controllable voltage source can take an external frequency as an input, with the external frequency being the output of the lumped dynamic model. The conversion method is based on identifying the voltage of the ac stiff voltage sources from the terminal voltages defined and the initial active/reactive power provided. The conversion method also needs to convert the per-unitized impedances to the actual impedances. Once the conversion of all the voltage sources in the equivalent circuit model is completed, the lumped dynamic model can be integrated into the local area dynamic model. Integrated dynamic models (i.e., ac grid models to integrate MARS at Pittsburg and Victorville, with 31 and 45 buses, respectively) were developed through this procedure. This process is summarized in Figure 2.

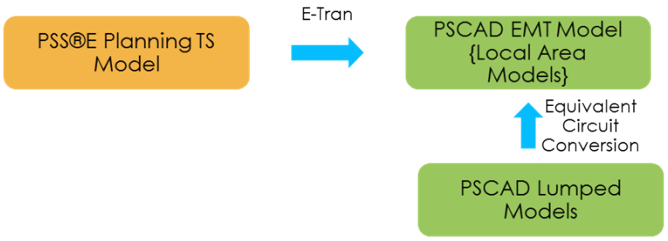

Figure 2. Integrated dynamic model development procedure.

The method can be utilized to develop EMT models of transmission grids in other studies, such as those performed by the North American Electric Reliability Corporation's (NERC's) Inverter-Based Resource Performance Task Force.

Milestone M 1.3, "Develop ac dynamic models with at least 30 buses," has been completed.

3.1.4 Develop Lumped ac System Models to Support the Studies and the Corresponding Use Cases

3.1.4.1 Events' identification in WECC 179-bus model

The analysis of the WECC 179 bus system aims to identify critical events when the MARS control system will be evaluated. MARS should be able to provide grid support under defined events. Two types of the events are applied to the two locations for installing MARS: Pittsburg, California, and Victorville, California. All events that lead to voltage and frequency deviations are summarized in Table 4.

Table 4. Contingencies analysis results summation.

Contingencies Type	Lost Generation (MW)	MARS Site of Interest	Voltage Magnitude Deviation (%)	Frequency Deviation (Hz)
L-L faults near LUGO	None	Victorville	14.96	N/A
L-L faults near SERRANO	None	Victorville	12.53	N/A
L-L faults near GATES	None	Pittsburg	12.5	N/A
TEVA TR generator loss	1,470.172	Victorville	N/A	0.08
Palo Verde generator loss	2,756	Victorville	N/A	0.16
HAYNES3 generator loss	804.4	Pittsburg	N/A	0.05

3.1.4.2 Evaluation of developed models

Based on the identified contingencies in WECC for the integration of MARS in Pittsburg and Victorville, the integrated dynamic models of the ac grids were evaluated. The reference models are based on considering a much larger portion of the ac grid in the local area dynamic models. The contingencies are based on the Blue Cut Fire that resulted in a line-to-line fault near Lugo, California, and a similar fault near Kirker, California. The results indicate that the developed models provide adequate representation of voltage and frequency variations, when compared with respect to the reference models (as shown in Figure 3). Further details of the model and more results may be found in [47].

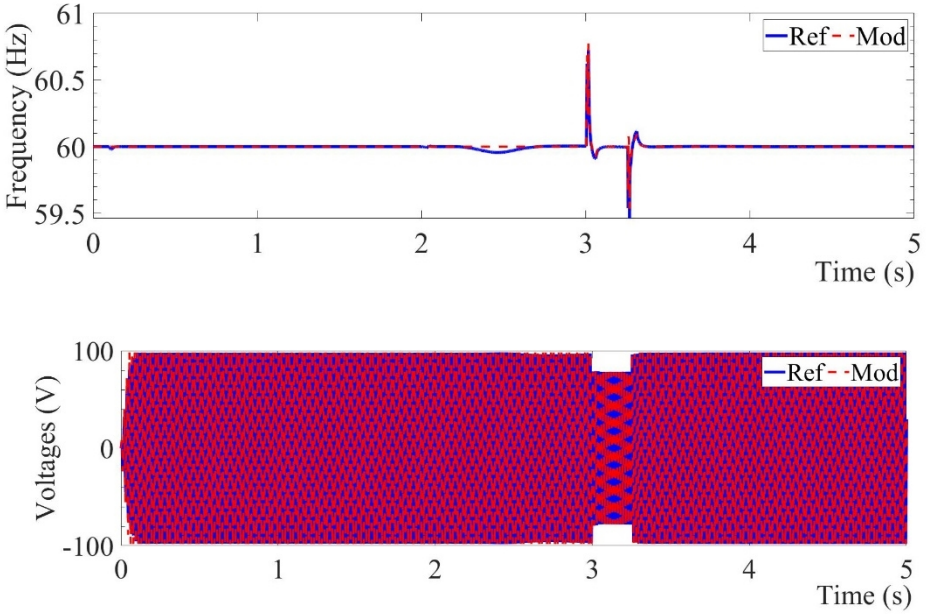

Figure 3. States measured at Pittsburg, California: (upper) frequency, (lower) voltage.

3.2 DESIGN AND DEVELOP REDUCED-ORDER MODEL OF MARS

3.2.1 Design MARS Circuit Based on the ESS and PV Plant Size

The MARS circuit architecture, shown in Figure 4, consists of six arms that connect to HVdc link and three phases of ac transmission grid. Each arm has "N" series connected SMs with an inductor. An SM in an arm can be a normal SM, a PV SM, or an ESS SM. There are "N_{normal}," "N_{pv}," and "N_{ess}" SMs per arm. The total number of SMs per arm "N" in MARS is determined by the dc-link voltage in the location and based on the installed HVdc substation. The number of each type of SM per arm depends upon the power and voltage rating of the PV arrays and energy storage connected. The circuit architecture of normal SMs can be a half bridge or full bridge, similar to an HVdc substation. The circuit architecture of a PV or an ESS SM will consist of the front-end circuit based on a normal SM and will have an isolated or nonisolated dc-dc converter connected to the front-end circuit. The parameters in each type of SM in MARS are obtained based on optimizing the cost and operational capabilities of MARS (e.g., range of operation, ripple in voltage/current). Based on this process, the circuit parameters of MARS are identified in Table 5 and Table 6 for MARS at Pittsburg. The parameters for MARS circuit at Victorville are sized similarly and can be found in Appendix A.1.1.

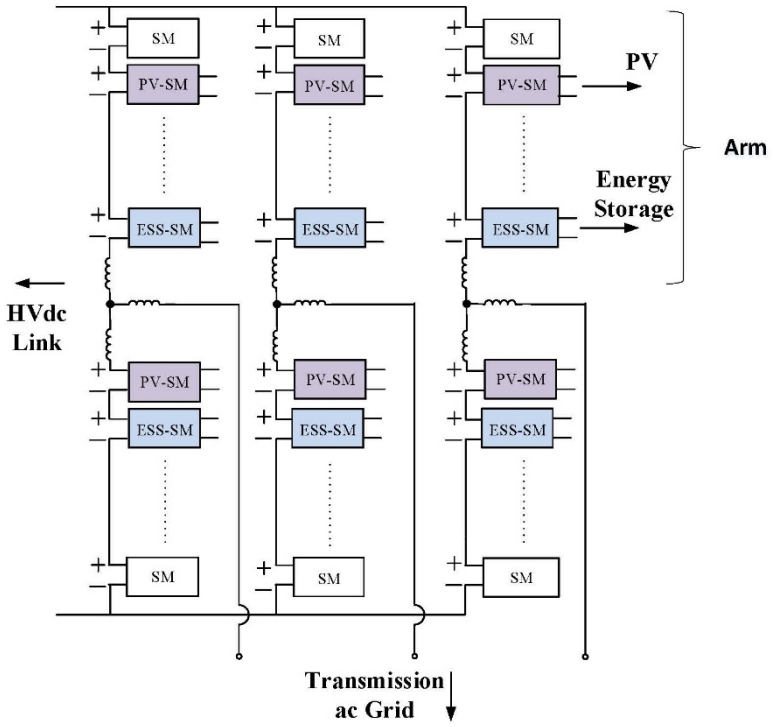

Figure 4. MARS circuit architecture.

Table 5. MARS at Pittsburg, California, circuit parameters.

Parameter	Value
Grid side inductance (L_s), mH	40
Grid side resistance (R_s), Ω	0.83333
Arm inductance (L_o), mH	30
Arm resistance (R_o), Ω	0.1
SM capacitor voltage (V_{sm}), kV	1.6
SM capacitor value, mF	7.7
PV system power rating (P_{pv}), MW	100
DC-DC converter input capacitor (C_{pv} & C_{ess}), mF	1
DC-DC converter inductor (L_{ess} & L_{pv}), H	0.0025
DC-DC converter switching frequency, kHz	10
No. of Normal submodules (SMs)	102
No. of PV SMs	111
No. of ESS SMs	37
Total no. of SMs	250

Table 6. MARS circuit details at Pittsburg, California.

Type of SM	No. of SMs (per arm)	Average SM capacitor voltage (per SM), V
PV	111	1,600
ESS	37	1,600
Normal	102	1,600
Total: N (per arm)	250	

3.2.2 Develop Reduced-Order Model of MARS Using Available Library in Commercial Software

The reduced-order model of MARS was developed based on equivalencing the MARS circuit's dynamic model and a part of the L1 controller. The equivalencing is based on averaging value methods and on the assumption of balanced SM capacitor voltages at a fixed value with negligible ripple. The reduced-order model of the system is summarized in Figure 5. The modulation indexes n_i^u and n_i^l, i = 1, 2, 3 are computed by part of the L1 controller implemented in the model. In the reduced-order model, the energy-balancing controller (EBC) and circulating current controllers are absent in the L1 controller because the SM capacitor voltage dynamics are ignored in the model.

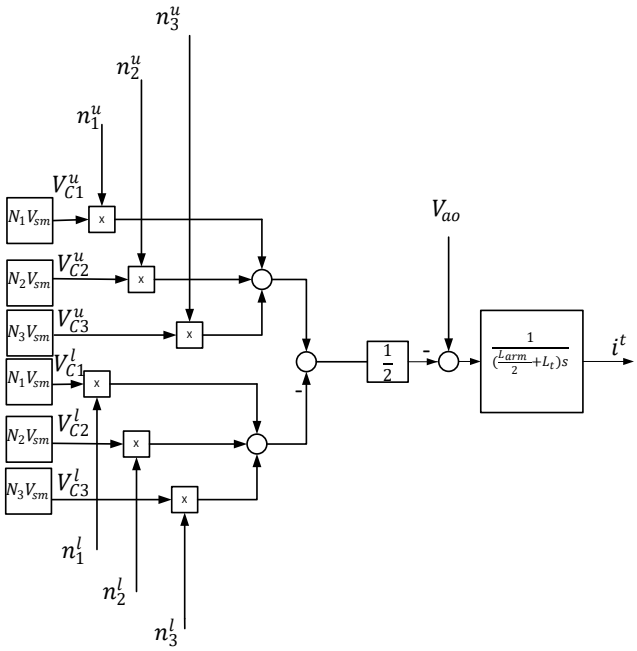

Figure 5. Schematic diagram of reduced-order model of one phase of MARS.

3.2.3 Evaluate and Validate the Reduced-Order Models

The simulated states from the reduced-order model are shown in Figure 6 along with high-fidelity model states. The results are similar to the high-fidelity model results (and within a 5% margin of error) for steady-state variables (ac-side currents, voltages, active power, reactive power).

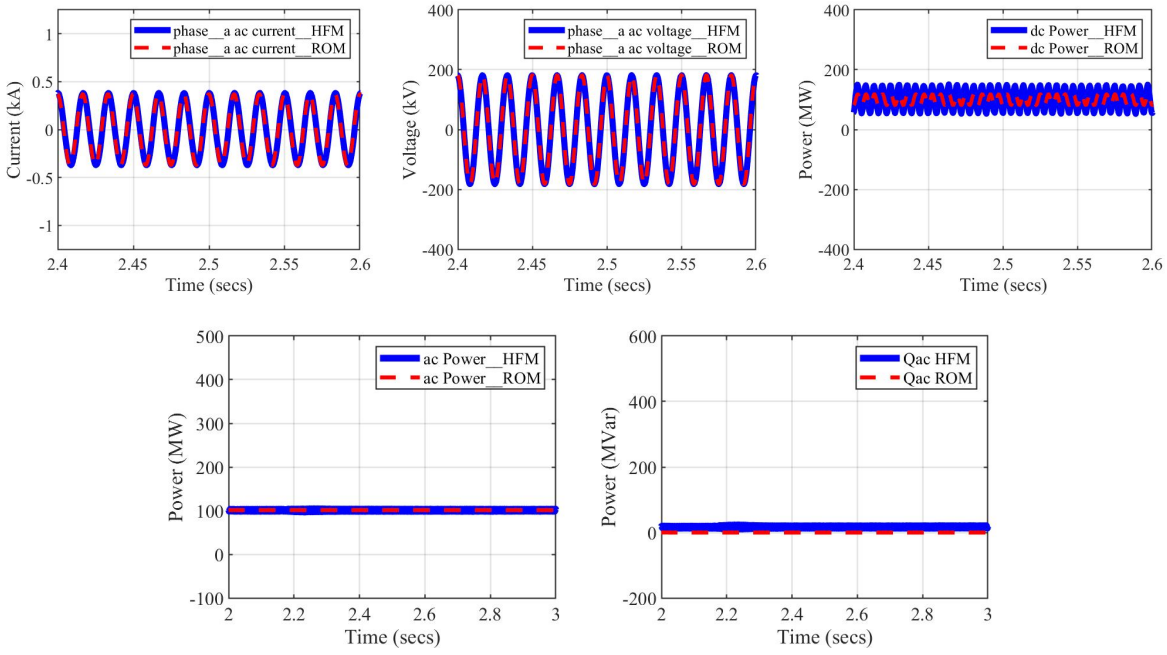

Figure 6. For the operating condition of P_{pv} = 32.8 MW, P_{ess} = -32.8 MW, P_{ac} = P_{dc} = 100 MW, and Q_{ac} = 0 MVAr, the states are displayed: (top left) Phase-a ac-side current; (top middle) Phase-a ac-side voltage; (top right) dc-side power; (bottom left) ac-side active power; and (bottom right) ac-side reactive power.

Milestone M 2.3, "Design and develop reduced-order model of MARS," has been completed.

3.3 DEVELOP SIMULATION ALGORITHMS AND HIGH-FIDELITY MODELS OF MARS

3.3.1 Develop High-Fidelity Models of MARS

A high-fidelity EMT model of MARS was developed based on switched system characteristics of all the power electronics components in the MARS system. The switched system characteristics are essential to identifying the transient stability challenges with inverter-based generations that are not captured with simplified average-value or active-reactive power (PQ) load model representation of inverter-based generations. The total number of states within the MARS system are $(18N_{\text{normal}} + 36N_{\text{pv}} + 42N_{\text{ess}}) + 6$. The number of states is on the order of thousands to tens of thousands. These states include the arm currents, normal SM capacitor voltages, PV SM capacitor voltages, PV SM inductor currents, ESS-SM capacitor voltages, ESS-SM inductor currents, and semiconductor switching states [48]. The equations representing the corresponding dynamics are shown in the Appendix A.2.1; the isolated module dynamics are shown here as an example. The high-fidelity EMT model of MARS also incorporates the discrete multi-rate hierarchical control system of MARS and its associated algorithms.

3.3.1.1 Isolated module

For the isolated module, the dynamics of the input-side capacitor voltage ($v_{\text{dcpv},y,l,j}$), ac currents in the module ($i_{\text{ac2},y,l,j}$), and front-end half-bridge capacitor voltage ($v_{c,y,l,j}$) are given by equation (2a), (2b), and (2c), respectively. In this example, differential algebraic equations representing the dynamics of some of the states show numerical stiffness (like ac currents), but the rest (capacitor voltages) do not.

$$C_{\text{dcpv}}\frac{dv_{\text{dcpv},y,l,j}}{dt} = -\frac{1}{R_{\text{dcpv}}}v_{\text{dcpv}} + \left(S_{\text{yl23,j}} \times S_{\text{yl22,j}} - S_{\text{yl24,j}} \times S_{\text{yl21,j}}\right) \times i_{\text{ac2},y,l,j} + \text{S}_{\text{BL2}} \times i_{\text{ac2},y,l,j} \times \text{sgn}\left(i_{\text{ac2},y,l,j}\right) + i_{\text{pv},y,l,j} \quad (2a)$$

$$L_t\frac{di_{\text{ac2},y,l,j}{}'}{dt} = \left(S_{\text{yl13,j}} \times S_{\text{yl12,j}} - S_{\text{yl14,j}} \times S_{\text{yl11,j}}\right) \times v_{\text{c},y,l,j} + \text{S}_{\text{BL1}} \times \text{sgn}(i_{\text{ac1},y,l,j})v_{\text{c},y,l,j} - a * \left(S_{\text{yl23,j}} \times S_{\text{yl22,j}} - S_{\text{yl24,j}} \times S_{\text{yl21,j}}\right) \times v_{\text{dcpv},y,l,j} - \text{S}_{\text{BL2}} \times \text{sgn}(i_{\text{ac2},y,l,j})v_{\text{dcpv},y,l,j} - i_{\text{acDAB2},y,l,j}{}' * R_t \quad (2b)$$

$$C_{SM}\frac{dv_{c,y,l,j}}{dt} = -\frac{v_{c,y,l,j}}{R_p} - i_{\text{acHB},y,l,j} + \left(S_{\text{yl23,j}} \times S_{\text{yl22,j}} - S_{\text{yl24,j}} \times S_{\text{yl21,j}}\right) \times i_{\text{ac2},y,l,j}{}' + \text{S}_{\text{BL2}} \times i_{\text{ac2},y,l,j}{}' \times \text{sgn}\left(i_{\text{ac2},y,l,j}{}'\right) \quad (2c)$$

where

$$S_{\text{BL1}} = \left(1 - S_{\text{yl11,j}}\right)\left(1 - S_{\text{yl12,j}}\right)\left(1 - S_{\text{yl13,j}}\right)\left(1 - S_{\text{yl14,j}}\right)$$

$$\text{S}_{\text{BL2}} = \left(1 - S_{\text{yl21,j}}\right)\left(1 - S_{\text{yl22,j}}\right)\left(1 - S_{\text{yl23,j}}\right)\left(1 - S_{\text{yl24,j}}\right)\ i_{\text{acHB},y,l,j} = S_{yl1,j}i_{y,j} + \left(1 - S_{yl1,j}\right)\left(1 - S_{yl2,j}\right)\text{sgn}(i_{y,j})i_{y,j}\ i_{\text{ac2},y,l,j}{}' = \frac{i_{\text{ac2},y,l,j}}{a}$$

$$\text{sgn}(x) = \begin{cases} -1\ if\ x < 0 \\ 1\ if\ x > 0 \end{cases}\ \forall\ y \in (p,n), \forall\ j \in (a,b,c), \forall\ l \in [1,N]$$

3.3.2 Develop Advanced Simulation Algorithms that Enable Fast Simulation of the High-Fidelity Models of MARS through High-Performance Computing Parallelization

The simulation of a high-fidelity EMT model of MARS is time-consuming because it involves a large number of states, the numerical stiffness associated with some of the states, and the small time-step requirements. Moreover, the use of a single conservative method of discretization in existing simulators (like PSCAD) makes it time-consuming. Hence, advanced EMT simulation algorithms such as numerical stiffness-based hybrid discretization, hysteresis relaxation technique [49, 50], and event-driven interpolation techniques have been applied. These algorithms are extremely critical for simulating high-fidelity models in a reasonable timeframe. They speed up the high-fidelity EMT model of MARS simulation by a factor of tens of thousands with respect to a baseline simulation model. The baseline simulation model was developed using existing simulator's library components (PSCAD) that represent the high-fidelity EMT model of MARS developed. The advanced simulation algorithms have inherent parallelism capability to exploit high-performance computing characteristics for real-time simulation.

Milestone M 3.2, "The preliminary developed simulation algorithm enables fast simulation," has been completed.

3.3.3 Integrate Simulation Algorithms to Simulate High-Fidelity Models Using Numerical Stiffness, Hybrid Discretization, and/or Multigrid Methods

The simulation algorithms that were developed were integrated in the MARS high-fidelity EMT models for both locations (Pittsburg and Victorville, California). The algorithm is summarized for reference in Figure 7.

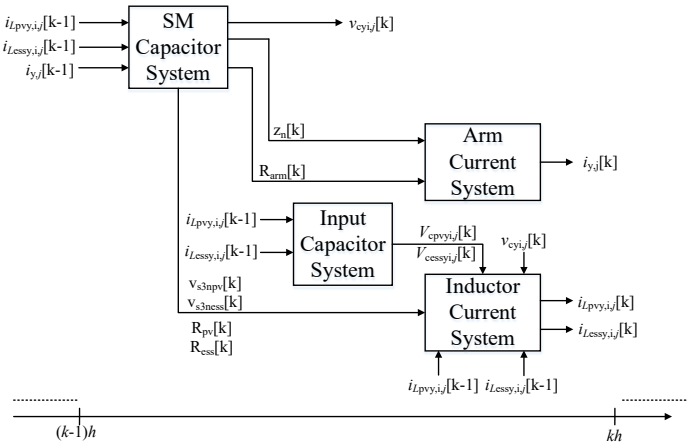

Figure 7. Detailed implementation of the MARS-HVdc simulation.

3.3.4 Test and Validate the Developed High-Fidelity Models

To validate the proposed simulation algorithms and the high-fidelity EMT model of MARS, a benchmarking case study of MARS based on the MARS system in Pittsburg, California, is considered here. The validation is with respect to the baseline model of MARS using the existing simulator's library (PSCAD). The dc link currents for two use cases that are shown in Figure 8, which indicate the developed high-fidelity EMT model (labeled "Developed Alg" in the figure), closely follow the results from the baseline model (highlighted as "PSCAD ref" in the figure). A relative speedup of up to 17,000× with an accuracy of >98% has been observed in the simulation of the developed high-fidelity EMT model of

MARS with the proposed simulation algorithms with respect to the baseline model of MARS [49, 50]. Further results are shared in Appendix A.2.2.

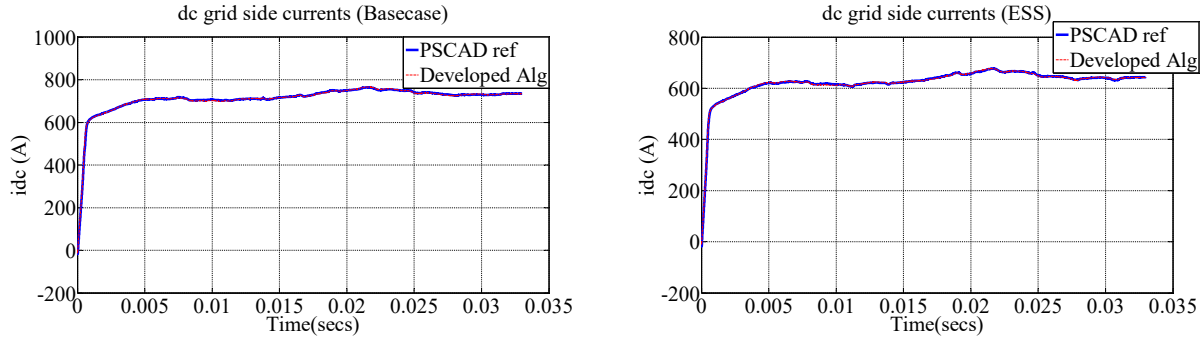

(a) (b)

Figure 8. Direct current bus current in MARS at Pittsburg (a) for base case (without PV and ESS power) and (b) for only ESS (with only ESS power generation).

The go or no-go decision point, M 3.4 G/NG-1, "Developed simulation algorithms and high-fidelity models for MARS," has been completed.

3.4 DESIGN AND DEVELOP OFF-LINE CONTROL ALGORITHMS IN MARS

The hierarchical control system of the MARS system is shown in Figure 9. In the figure, the measured parameters of MARS circuit hardware are shown in the "Measurement" column (along with the medium of data transfer), the hierarchical control system is shown in the "Controller" column (with the data exchange between each layer of the controller and the medium of data transfer), and functions of each control layer in the hierarchical control system are shown in "Functionalities" column. The functionalities include PQ control, current control, dc link voltage control, virtual synchronous generator (VSG) control, EBC, capacitor voltage balancing, and power and current control in the PV/ESS. The L1 controller is implemented in a central processing unit (CPU) at a 60 µs time step (or similar), the L2 controller is implemented in a field-programmable gate array (FPGA) at a 4 µs time step (or similar), and the L3 controller is implemented in digital signal processors (DSPs) at a 100 µs time step (or similar). The CPU-FPGA is implemented in two cores and a Kintex-7 FPGA; the DSP is based on F28335.

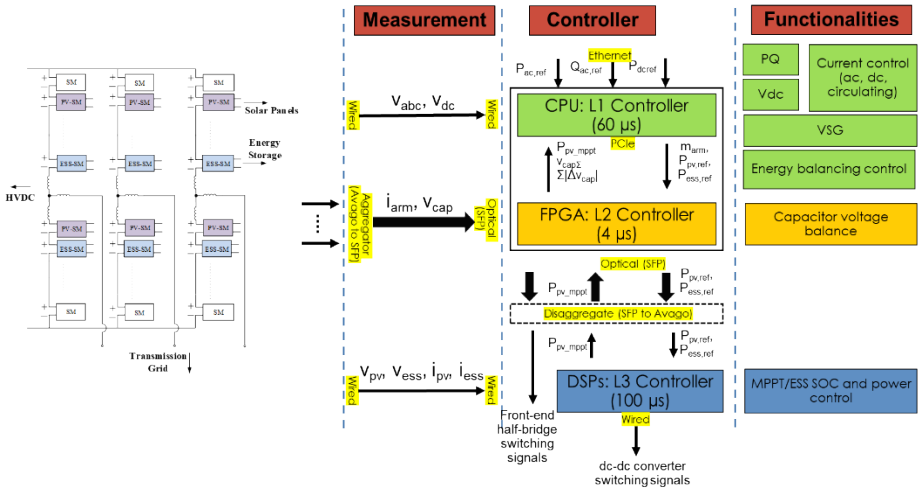

Figure 9. MARS control system.

3.4.1 Integrate Reduced-Order Models of MARS with ac Dynamic Models

The reduced-order model of MARS and ac grid were developed and implemented in the Matlab/Simulink software environment. The developed reduced-order ac grid model, as shown in Figure 10**,** consists of a frequency-controlled voltage source and 2 pi-line sections representing the transmission line. While the frequency-controlled voltage source represents the frequency dynamics of the bulk power system during a loss-of-generation event, the 2 pi-line sections equivalently represent the short-circuit ratio (SCR) of the system and provide capability to test fault events in the grid.

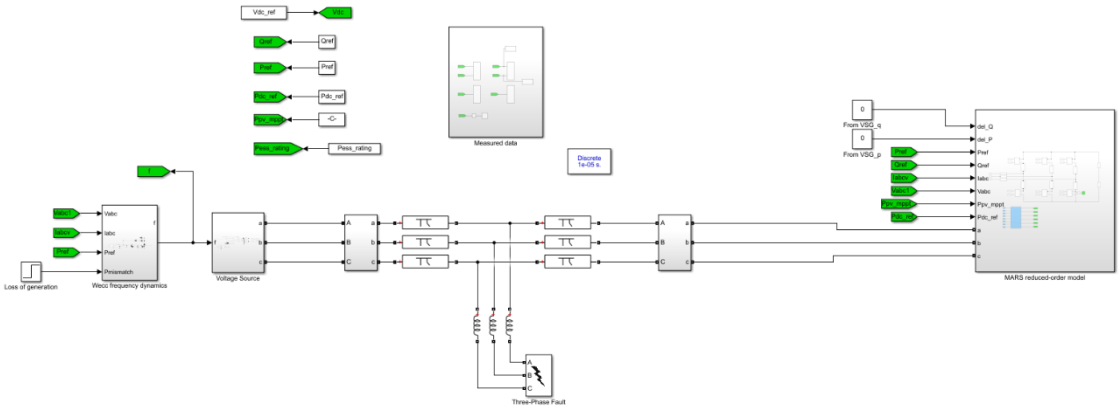

Figure 10. MARS reduced-order model integrated with the reduced-order ac grid model in MATLAB/Simulink.

3.4.2 Develop Virtual SG Algorithms to Support Frequency and Voltage

The frequency-power response (FPR)–based control method is one of the approaches to implement the desired VSG features for renewable power plants. The active power output of the VSG controller in response to a frequency disturbance in the system can be expressed as

$$P_{\mathrm{VSG}} = K_D \Delta\omega + K_{\mathrm{I}} \frac{d\Delta\omega}{dt} \tag{3}$$

where Δω and dΔω/dt represent the change in angular frequency and the corresponding rate of change of frequency (ROCOF). K_{D} and K_{I} represent the damping and the inertial constants, respectively. K_{D} is similar to the frequency droop and helps return the frequency to a steady-state value and reduce the frequency nadir. K_{I} arrests the ROCOF by providing a fast dynamic frequency response based on the frequency derivative. The performance of the implemented VSG control in the L1 controller has been verified in the MARS reduced-order model, shown in Figure 11. It shows the frequency nadir improvement by up to 12.5% with the VSG controller in MARS (as compared to without the controller).

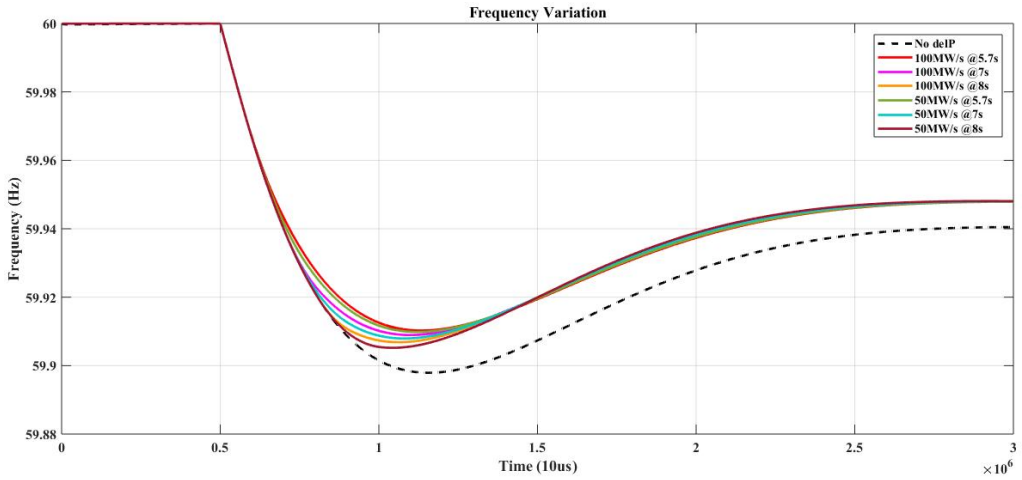

Figure 11. Frequency measured upon loss of Haynes3 generation (dashed line: no support from MARS; solid line: support from MARS with different ramp rates from active power and at different detection rates of the loss of generation).

In addition to VSG control, a grid-forming phase locked loop (PLL)-less control called as synchronous generator (SG)-based control based on swing equation dynamics and model predictive control (MPC)-based SG control methods are developed. The detailed description is provided in Appendix A.3.1.

Milestones M 4.2, "Preliminary results from developed control algorithms in MARS," has been completed.

3.4.3 Develop Harmonized Source Control Methods

To balance the energy across different types of SMs (PV, ESS, normal) within each arm of MARS, the currents of the arms are augmented with an additional fundamental frequency ac component (that is circulating). This requires the EBC that uses the voltages measured across the capacitors within the SMs in each arm to generate the circulating current reference that is fed to the circulating current controller that also ensures removal of second and fourth harmonic circulating currents. The overall MARS lower-level control method to harmonize resources (PV, ESS) is shown in Figure 12. The capacitor voltage-balancing algorithm in the L2 controller is upgraded in MARS as compared to the traditional HVdc substation's algorithm to accommodate PV and ESS resources within MARS. The algorithm is shown in Figure 13**.** The power and current controllers in each ESS SM and the voltage and current controllers in each PV SM in the L3 controllers are described in Appendix A.3.2.

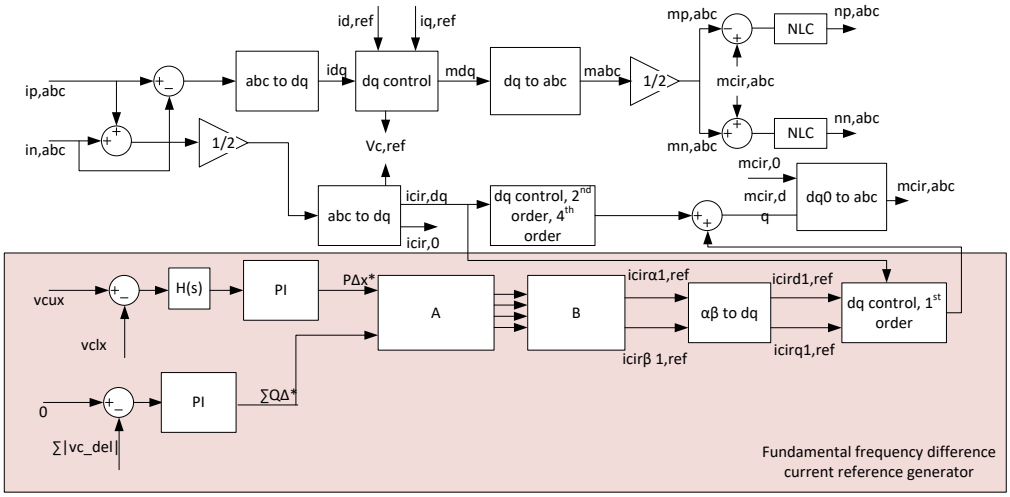

Figure 12. MARS lower-level L1 control (EBC, circulating current control, ac-side current control).

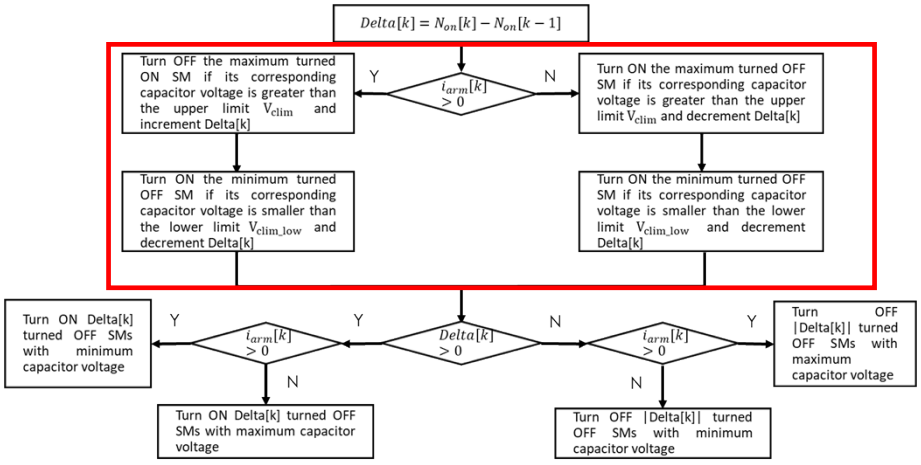

Figure 13. The upgraded L2 controller algorithm.

3.4.4 Test and Validate Developed Algorithms

The hierarchical control system of MARS in Pittsburg, California, consists of L1, L2, and L3 controllers operating at different time steps. The L1 controller operates at 60 µs, L2 controller operates at 4 µs, and L3 controller operates at 100 µs. The multi-rate controllers along with the measurement/communication delays are incorporated in the multi-rate hierarchical control system model implemented within the high-fidelity EMT model of MARS. The data exchange between each controller and modules at each time step is shown in Figure 9. This model is integrated with the EMT ac grid model developed for the Pittsburg region in Task 1.

3.4.4.1 Simulation results and test cases for high-fidelity EMT model of MARS with developed EMT grid models

Four use cases were identified and tested in this study:

1. Stability tests under the following operating conditions.:
   a. P_{ac} = –30 MW and P_{dc} = 100 MW

   b. P_{ac} = –100 MW and P_{dc} = 30 MW
2. 804.44 MW loss of generation in WECC for the following operating conditions:
   a. $P_{ac} = P_{dc}$ = 100 MW
3. 3-phase fault for the following operating conditions:
   a. $P_{ac} = P_{dc}$ = 100 MW
4. Line-line faults for the following operating conditions:
   a. $P_{ac} = P_{dc}$ = 100 MW

Stability tests

The control system of MARS was tested under different operating conditions. The SM voltages of each type of SM for the operating conditions are shown in Figure 14(a) and (b). The voltages are stable around the nominal SM voltages (1600 V); no over-voltages (of greater than 2000 V) or under-voltages (of less than 1200 V) are observed.

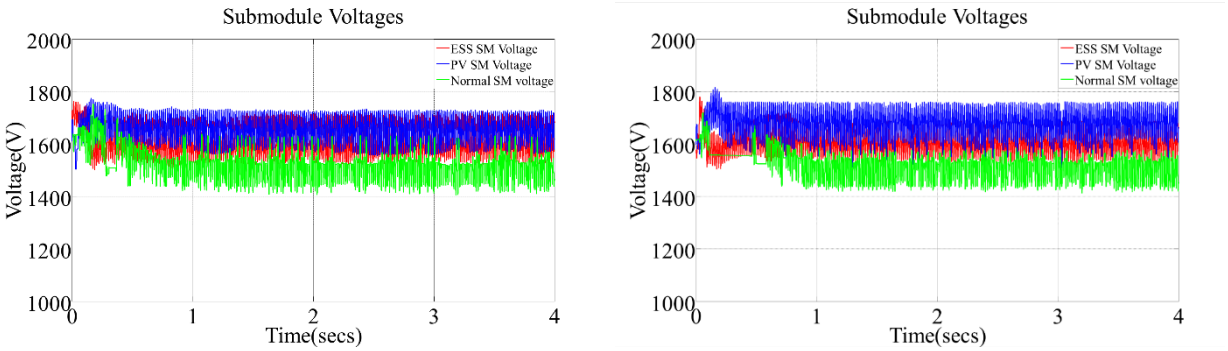

(a) (b)

Figure 14. SM capacitor voltages for the following operating conditions: (a) P_{ac} = -30 and P_{dc} = 100 MW, (b) P_{ac} = 30 MW, and P_{dc} = -100 MW.

804.44 MW loss of generation

An event of 804.44 MW loss of generation was simulated at t = 2.0 s. The frequency response measured at Pittsburg with and without VSG support from MARS is shown in Figure 15. The results illustrate the improvement in frequency nadir by 20.23% and in steady state frequency response by 21.20%.

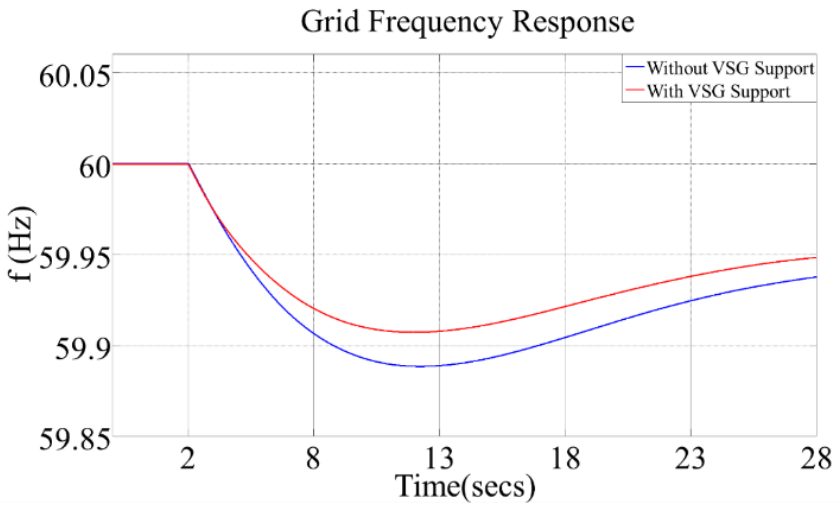

Figure 15. Grid frequency response for 804.44 MW loss of generation in WECC grid for operating condition $P_{ac} = P_{dc} = 100$ MW.

Three-phase fault

A three-phase fault was simulated on a transmission line in the developed EMT model of the grid at t = 3.5 s with the fault duration of 0.25 s. After 0.25 s, the fault is self-cleared. The ac-side grid voltage's magnitude, active power provided by MARS, and reactive power support from MARS during the fault with and without VSG support are shown in Figure 16(a)–(c). The improvement in the voltage profile with the VSG support is 31.48%. The active power provided by MARS is improved by 40.78% with VSG support.

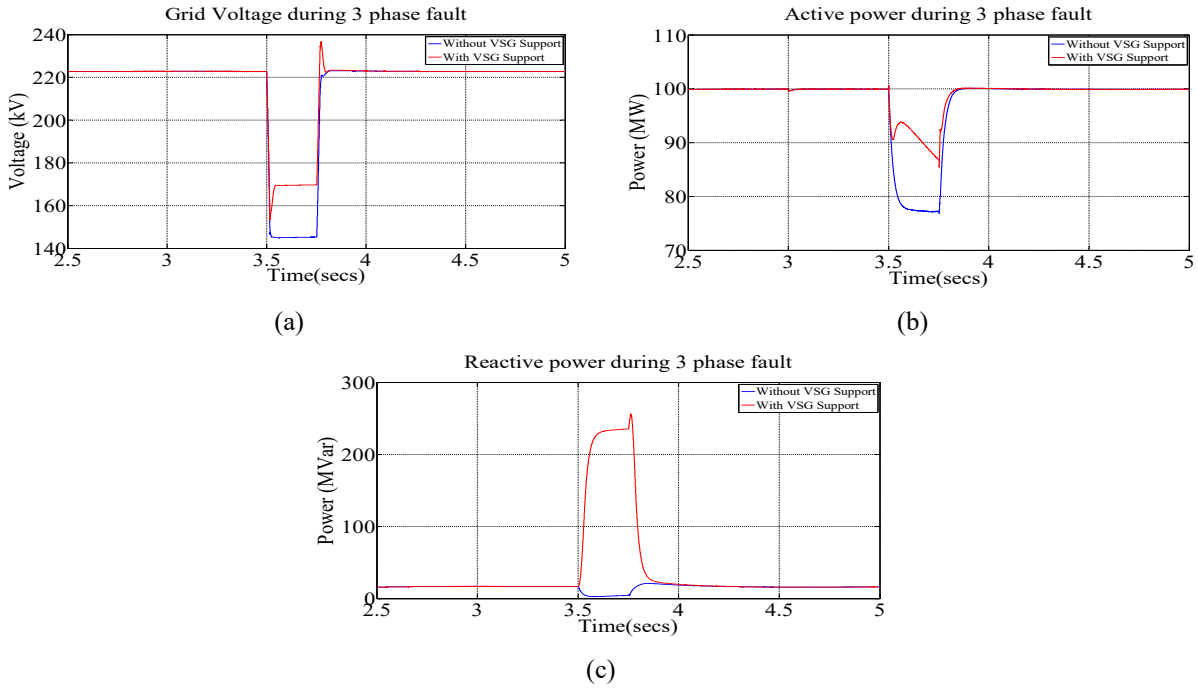

Figure 16. During three-phase fault: (a) ac side grid voltage's magnitude, (b) active power support, (c) reactive power support.

Line-line phase fault

A line-line fault is simulated at t = 8.0 s with the fault duration of 0.25 s. The fault self-cleared after 0.25 s. The fault is between phases *a* and *b*. The ac-side grid voltage's magnitude, active power provided by MARS, and reactive power support from MARS during the fault with and without VSG support are shown in Figure 17(a)–(c). The improvement in the voltage profile with the VSG support is 58.5%. The active power provided by MARS is improved by 65.21%.

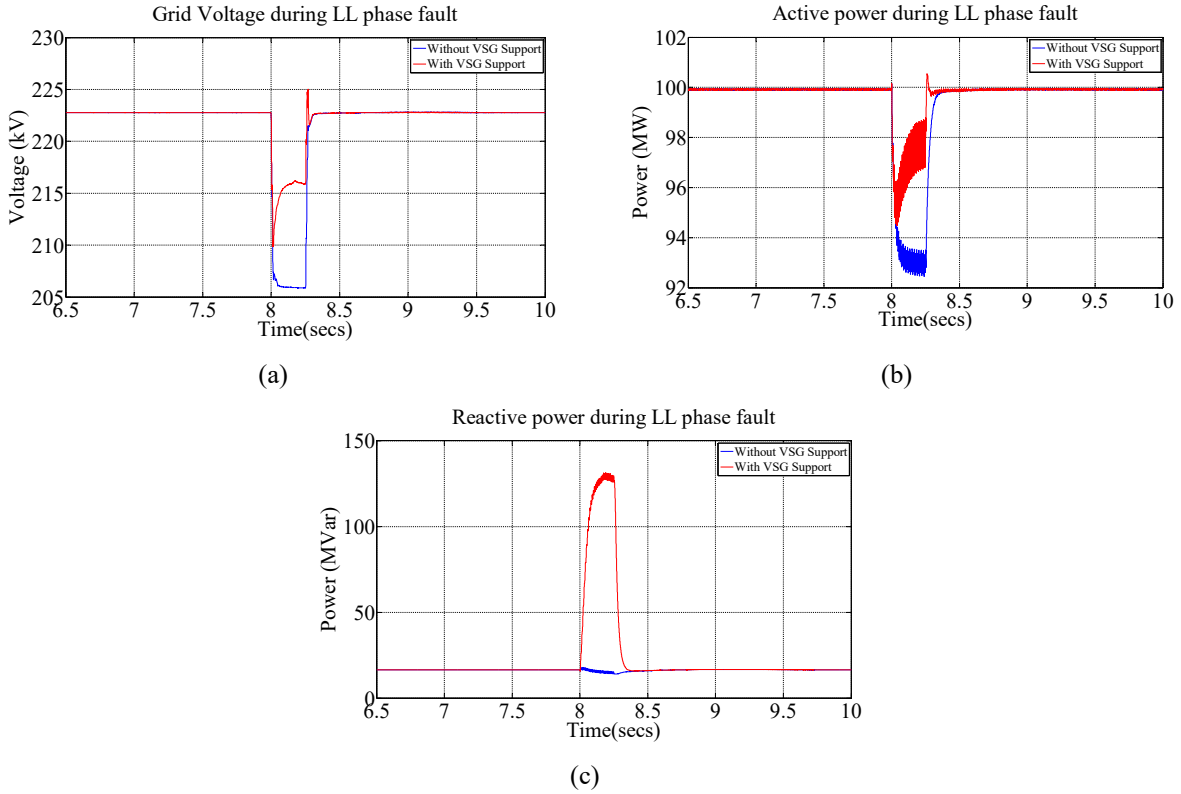

Figure 17. During line-line phase fault: (a) ac side grid voltage's magnitude, (b) active power support (c) reactive power support.

Disturbance rejection was observed in all use cases tested. Additionally, based on existing analysis [51, 52], it has been identified that congestion can be mitigated using MARS-type systems through the HVdc links at least 2%.

3.4.5 Develop a Preliminary Business Model for the MARS Plant

3.4.5.1 Business case study estimation

The electrical system configuration of the baseline case is illustrated in Figure 18. The main electrical components include PV and ESS inverters, step-up distribution transformers, circuit breakers, collection grid cables, transmission substation apparatus (power transformers and circuit breakers), and an HVdc converter station.

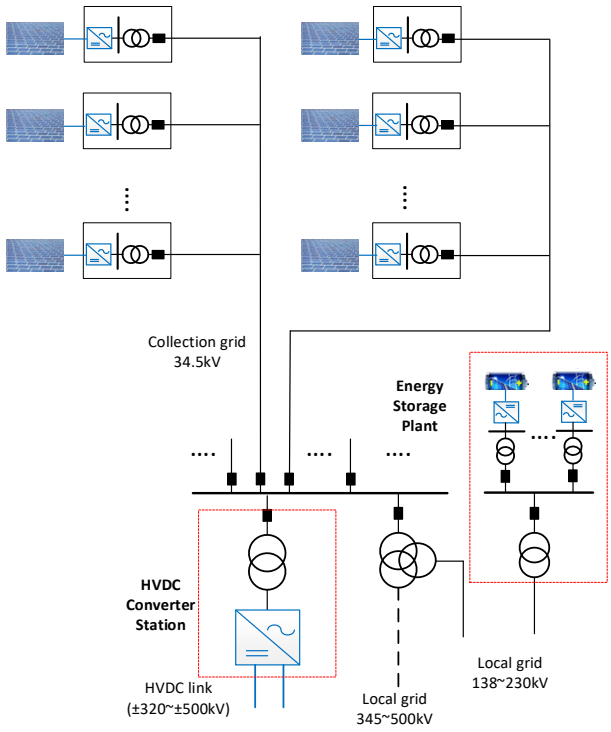

Figure 18. Illustration of the baseline electrical system configuration.

The electrical system configuration of the integrated MARS design is illustrated in Figure 19. The main electrical components include PV, ESS, and normal SMs; low-voltage direct current (LVdc) circuit breakers (not shown in the figure); collection grid HVdc cables; transmission substation apparatus (transformers and circuit breakers); and dc auxiliary apparatus (not shown) to support series connection of SMs and HVdc link operation.

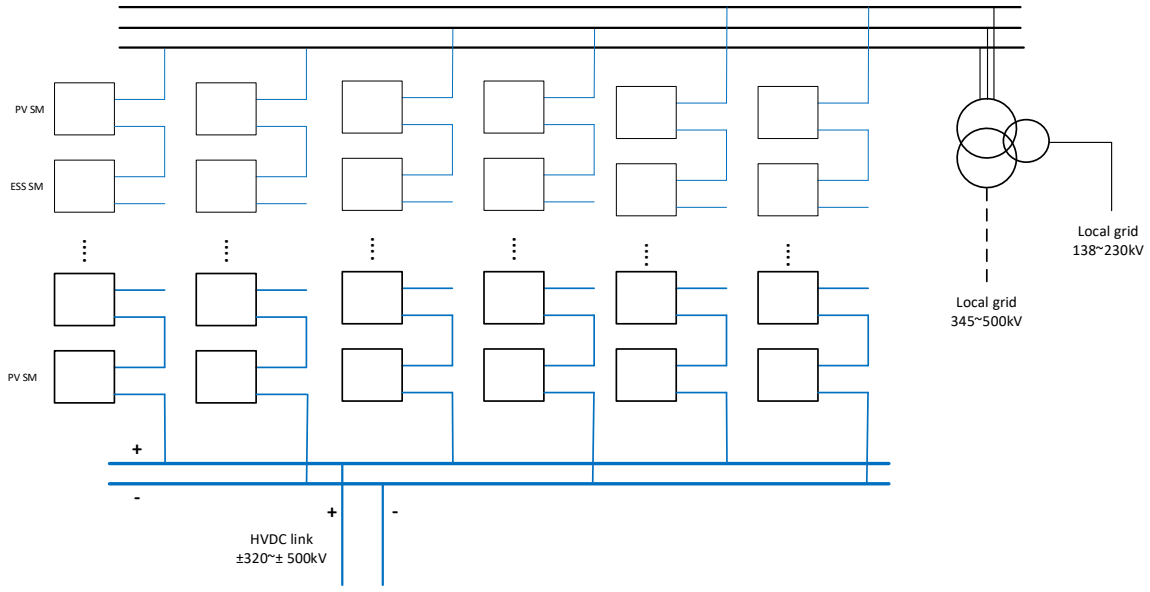

Figure 19. Illustration of the MARS electrical system configuration.

The preliminarily calculated electrical system costs of a gigawatt-scale PV-plus-storage system are calculated based on the system design parameters and the component cost data from public-domain records [53–56]. The components considered for the cost analysis include power electronics inverters, circuit breakers, collection cables, substation equipment (power transformers and breakers), an HVdc substation, control systems, and miscellaneous costs. In addition to the electrical costs, the soft and module costs are calculated to identify the capital cost of each design. The operations and maintenance (O&M) costs, transmission costs, and net energy production are considered to identify the levelized cost of each design. The levelized cost of electricity (LCOE) for each design (baseline and integrated systems) is calculated as follows:

$$\text{LCOE} = \frac{\text{Lifecycle cost of solar project}}{\text{Lifecycle energy prodcution of solar project}}$$

$$= \frac{\text{Capitial cost} + \text{O\&M cost} + \text{transmission cost}}{\text{Net energy production}}$$

The levelized O&M costs and transmission costs are estimated from [54]. The net energy production is based on 12 h base-load generation profiles of the PV-ESS combined system identified in Task 1 and the efficiency of energy transmission of each design. The efficiency of the baseline design is estimated based on PV inverter, ESS inverter, HVdc converter and filters, step-up power transformer, and cable efficiencies. The efficiency of the integrated MARS design is estimated based on SM, cable, and transformer efficiencies. The estimated baseline and integrated efficiencies have shown up to 50% improvement in efficiency. The efficiency of the state-of-the-art design is assumed to be similar to that of the baseline design in this study. The state-of-the-art design uses a PV plant, ESS plant, and additional synchronous condensers/transmission lines upgrades.

A preliminary business case has been provided that show there is reduction in electrical cost in the system with respect to the baseline case study (as well as the state-of-art design). The reduction in this cost for integrated development is based on the integrated PV-ESS system considered in [53]. The reduction in electrical costs is on the order of up to 50% in the preliminary analysis. Additional costs from switchyard and enclosures were included in the analysis in the next sections. The reduction in levelized costs were also identified in the preliminary analysis.

The go or no-go decision point, M 4.5 G/NG-2, “Design and develop control algorithms in MARS. Preliminary business model presented,” has been completed.

3.5 MODEL CYBER VULNERABILITIES AND DESIGN CYBER PROTECTION

3.5.1 Develop Two Test Cases to Study Vulnerabilities in MARS.

The test cases to study vulnerabilities in MARS have been identified. In the hierarchical control system in MARS, a false data injection attack (FDIA) seems to be one of the potential cyber-attacks because the system is localized and does not use a global positioning system and. Based on the likelihood of an FDIA-type attack, two types use cases (with a total of six use cases based on individual command or measurement affected) were formulated.

3.5.2 Model Cyber Vulnerabilities

Two critical failure scenarios in the L1 controller that result from malicious commands and measurements were identified, and the corresponding impacts were assessed.

Milestone, M 5.0, “Developed test cases for MARS vulnerability assessment,” has been completed.

3.6 DESIGN PE MODULE

3.6.1 Design Power Electronics Hardware-in-the-Loop Concept to Emulate MARS

The power electronic hardware-in-the-loop (PE-HIL) concept to emulate MARS has been designed such that the SM's controller (the L3 controller) in MARS can be evaluated. When the numerical stiffness-based hybrid discretization is used to segregate the dynamics within the SM from the rest of MARS, one of the SM's L3 controllers can be integrated and tested with the rest of the MARS hierarchical control system (L1-L2).

3.6.2 Design Gate-Drivers, Sensors, and a Communication System in SMs

An interface board connects the gate-drivers and sensors from PV and ESS SMs to the hierarchical control system of MARS. The printed circuit board designed for the interface board is shown in Figure 20. The interface board extends the input/outputs (I/Os) of the DSP controller (the L3 controller) with fiber-optic transmitters/receivers and supplies power to the SMs' components. The fiber-optic receivers and transmitters are used to provide communication with the L2 controller.

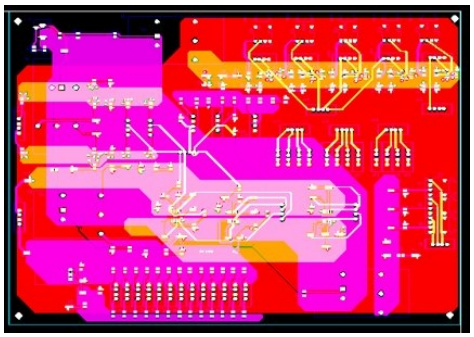

Figure 20. The printed-circuit board design for the interface board.

3.6.3 Design Semiconductor Devices and Heat Sinks for PE Module's Design

The semiconductor devices, capacitors, inductors, heat sinks, gate drivers, fans, voltage sensor, current sensor, interface board, and other components were identified for the ESS SM. A 3D diagram was developed for the SM. The preliminary theoretical efficiency calculated for the module (as shown in Figure 21) and for MARS is greater than 95%.

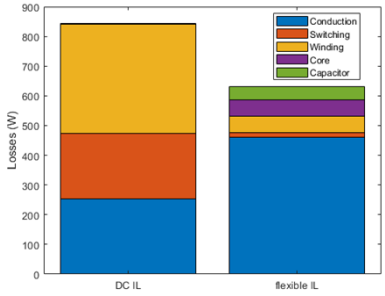

Figure 21. Loss analysis in an ESS DC-DC converter.

The go or no-go decision point, M 6.0 G/NG-3, "Designed PE module," has been completed.

3.7 DESIGN CONTROL AND HIL PLATFORM

3.7.1 Design Real-Time Simulation Hardware Based on AC System Models

Real-time simulation hardware requirements were identified for the HIL testing of MARS. The real-time simulation requires CPUs to simulate an AC grid model and a MARS ac interface model. The simulation time step is 60 µs. The largest AC grid model used for the real-time simulation consisted of 30 buses, 45 lines, 45 transformers, and other components. The OP5707 real-time simulator from Opal-RT was used; up to three cores were identified for the simulation of the MARS AC interface and AC grid model. A Virtex7 FPGA was used to model the normal SMs, PV SMs, and ESS SMs, which are on the order of several thousands of modules in total.

3.7.2 Design Hierarchical Control Hardware Based on Control Algorithms

The MARS hierarchical control system consists of a CPU, an FPGA, and DSPs, as discussed in Task 4. The hardware components identified for the L1 and L2 control systems are the CPU and Kintex7 FPGA, respectively, in OP4510. The Texas Instruments F28335 DSP is the L3 control system hardware component.

3.7.3 Design MARS HIL

The overview of the HIL for MARS is shown in Figure 22. The MARS hierarchical control system (L1-L2) and real-time simulation hardware will be interconnected to each other with small form-factor pluggable (SFP) fiber optics and copper conductors to send various measurement signals from the hardware to the L2 controller and gating signals from the L2 controller to the hardware. The L1 controller is connected to the L2 controller from peripheral component interconnection express (PCIe). This architecture can also be extended to include one real L3 controller hardware connected to the real-time simulator.

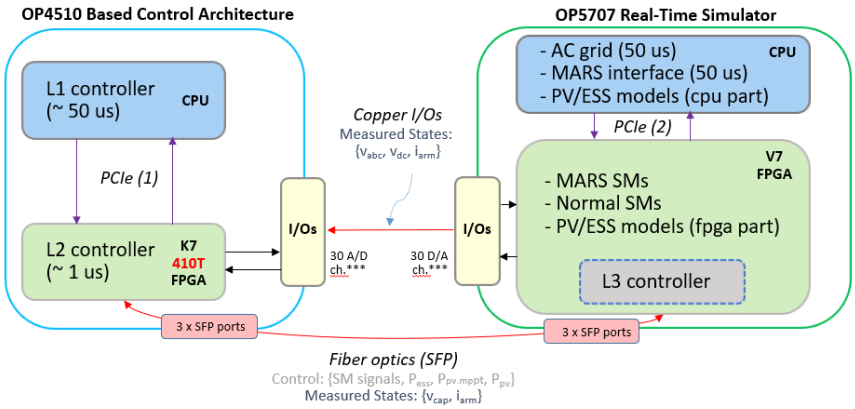

Figure 22. HIL design architecture for testing the MARS hierarchical control system.

The go or no-go decision point, M 7.0 G/NG-4, "Designed HIL and control platforms," has been completed.

3.8 DEVELOP HIL AND CONTROL PLATFORMS

3.8.1 Develop the Hierarchical Control Platform

The hierarchical control platform of MARS in OP4510 (CPU-FPGA) was tested and evaluated for real-time performance quantification of the communication hardware. For example, a simple loopback was performed with one-bit switching signal transmitted through one SFP channel in the OP4510 and then received through another SFP channel. The switching signals transmitted to the SFP channel and received at the SFP channel were both sent to the digital outputs. An oscilloscope was then used to measure the latency between these two switching signals from the digital outputs. The latency in this SFP communication was measured between 546 and 596 ns, which was close to the expected theoretical latency of 500 to 600 ns. Additionally, the non-SFP fiber-optic ports for connection to the DSP were also evaluated. During benchmarking, the latency was measured when these ports were operated as digital I/Os. After setting up the loopback, the latency measured in this optical port was 74 ns, which is not a significant delay between the DSP and the FPGA of the MARS hierarchical control platform.

3.8.2 Develop the MARS HIL Platform

In the MARS HIL tests, three SFP channels will be used between the control platform and the MARS HIL platform. The size of the data transmitted per SFP channel from the control platform to the MARS HIL platform will be 314 words, each word being 32 bits in size. They include the switching data and power commands to PV and ESS. The size of the data transmitted from the MARS HIL platform to the control platform will be 609 words per SFP channel. The data include measured voltages and currents. The identification of latency for an SFP channel in sending a one-bit switching signal from the control platform to MARS HIL platform, comparison of analog signals before transmitting and after receiving, and identification latency for SFP channel in MARS HIL platform as found by loopback test using full-size of data package are also performed. The results of analog signals, shown in Figure 23, do not show mismatches between signals (and this was observed in other tests too). The latency measured from switching signals is between 5.28 and 6.10 µs, as shown in Figure 24.

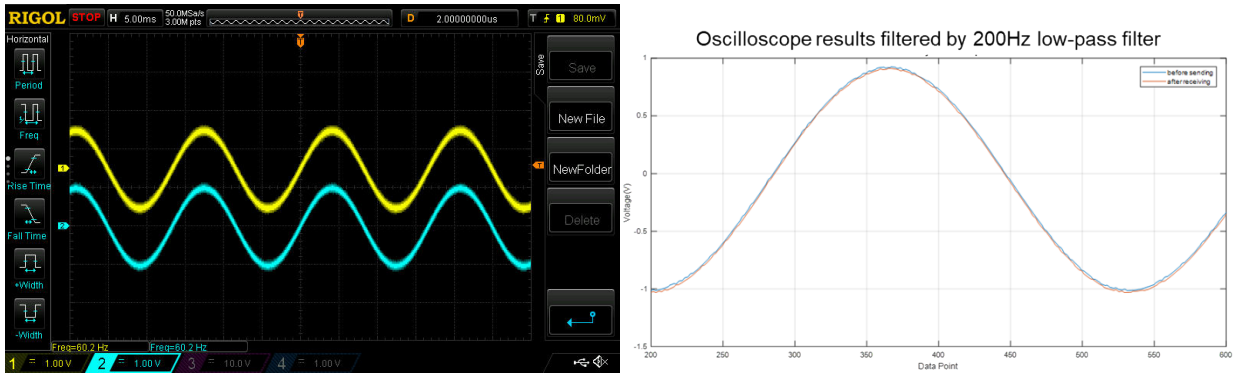

Figure 23. Comparsion of analog signals before transmitting and after receiving.

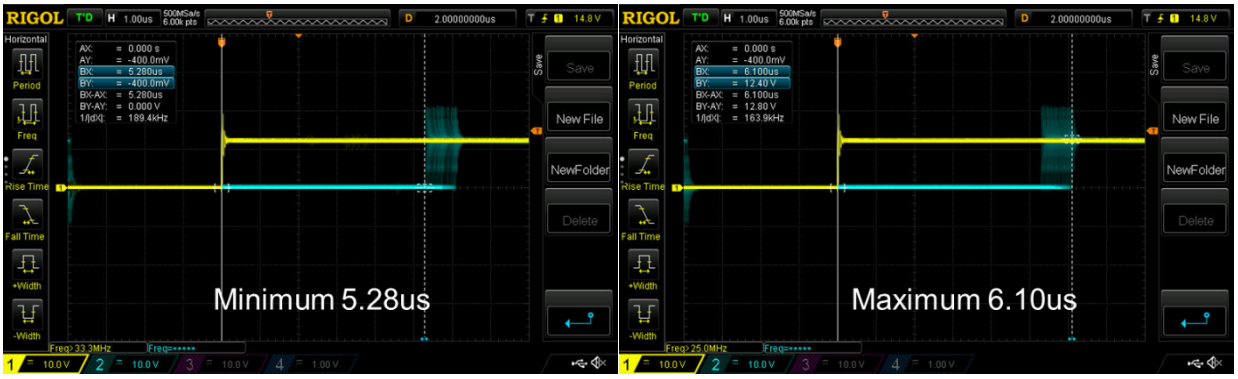

Figure 24. Latency for SFP channel in OP5707 as found by loopback test using the full size of the data package.

3.8.3 Develop the AC System Real-Time Simulation Platform

The IEEE 39-bus grid model was selected for benchmarking because it has the similar characteristics of the ac grid model used in the MARS case study. To evaluate the real-time performance, the computation time of each element in the IEEE model was identified. The total computation time of the IEEE model was calculated by summing the computation times of evaluating the dynamics of individual elements. Thereafter, the complete model was simulated in real time, and its total computation time was recorded. In this benchmark, the total computation time calculated from the individual components in IEEE 39-bus model was 65.03 µs, and the computation time recorded was 64.97 µs. The two computation times indicate that the calculated computation time is close to the measured computation time for the real-time simulation of this ac system.

The ac grid model was intended to run in the MARS HIL platform with a time step of 60 µs. Based on the benchmarking, it was observed that the CPU use of the platform will satisfy this need if the model is run in two CPU cores. In such scenario, after implementing the ac grid model, the simulator will still have approximately 24.64 µs for overheads and any additional computation/operations.

Milestone M 8.0, "Develop HIL and control platforms," has been completed.

3.9 IMPLEMENT REAL-TIME PE-HIL ALGORITHMS

3.9.1 In Developed HIL Platform, Optimize and Implement the MARS Models and Simulation Algorithms to Ensure Real-Time Operation

The dynamics of the SMs (normal, PV, and ESS) in MARS are implemented in the FPGA of the MARS HIL platform. The challenges arise with the very large number of SMs present that need to be simulated in real-time and using a small time step. Using individual converter models from the library (existing) can be prohibitive for real-time simulation. Therefore, the parallelism identified in Task-3 is utilized in the real-time simulation through pipelining and optimization of resources in the FPGA to optimize the implementation. The MARS ac-side interface in the CPU is implemented based on Opal-RT's existing MMC toolbox. This interacts with the SMs' dynamics in the FPGA. The models and simulation algorithms used for MARS' real-time simulation is based on the developments in Task-3 for offline simulations. The overview of this implementation is shown in Figure 25.

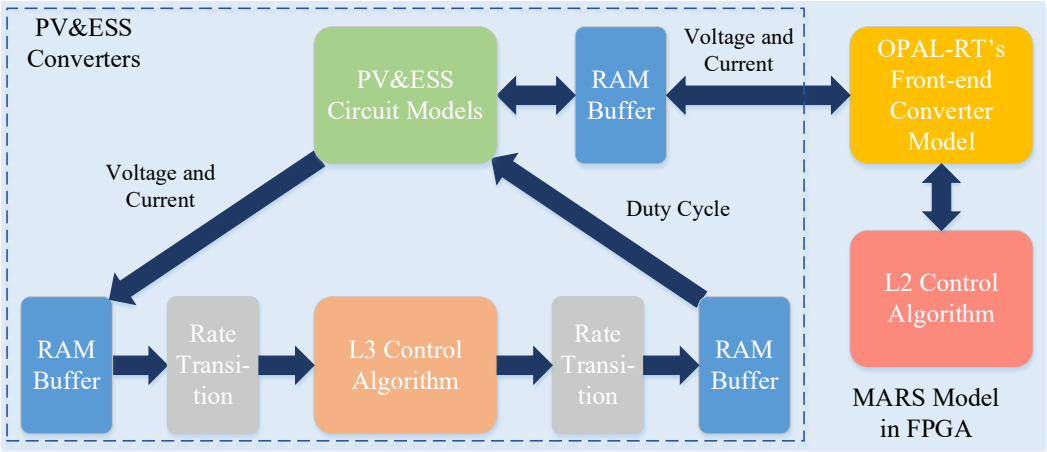

Figure 25. Structure of real-time simulation model of MARS developed in the FPGA.

The real-time performance was shown to be successful under different operating conditions and with normed errors less than 5% in voltages and currents in PV and ESS SMs that are non-isolated. One of the test results is shown in Figure 26. The real-time simulation of MARS was performed for different numbers of modules in MARS for an example test system with fewer PV and ESS SMs in MARS and for MARS at Pittsburg.

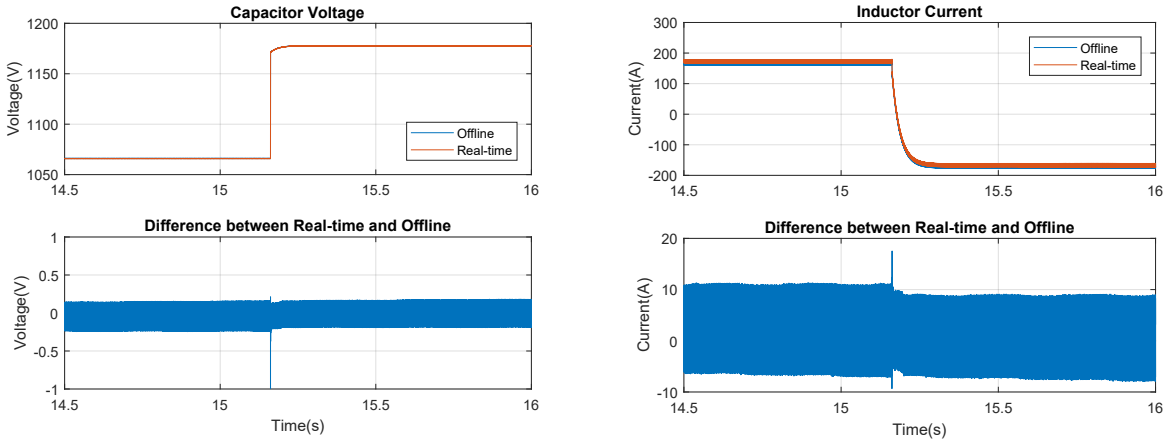

(a) (b)

Figure 26. Real-time and offline simulation of (a) capacitor voltage and (b) inductor current results of the ESS model after a step change of reference.

3.9.2 Integrate Communication Algorithms to Exchange Data from Real-Time Simulation of MARS with the Control Platform and AC System Real-Time Simulation

Based on the hierarchical control platform of MARS, the SFP communication and analog I/Os were utilized between the MARS cHIL setup and the control platforms. This is shown in Figure 27.

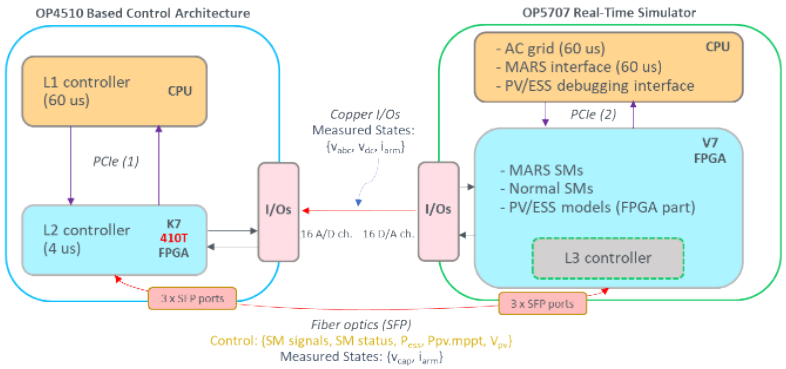

Figure 27. Structure of the MARS cHIL setup.

In the SFP communication algorithm, the data were exchanged bidirectionally between MARS HIL simulation and control platforms. The generic SFP communication design with six channels was modified into three channels for the control platform designed for MARS specifically through a needed algorithmic update.

The L2 control algorithms in the control platform were tested in real time through an HIL based on the developed real-time HIL simulation model of MARS. In this case, the L3 controllers were implemented within the FPGA of the MARS HIL platform and a generic L1 controller was implemented in the CPU of the control platform. The test results are shown in Figure 28, and they are as expected (with similar results observable in offline simulations). The as-expected test results showcase the successful establishment of the communication between the control platform and MARS HIL platforms with small latency. They also showcase the accuracy of the real-time MARS simulation model.

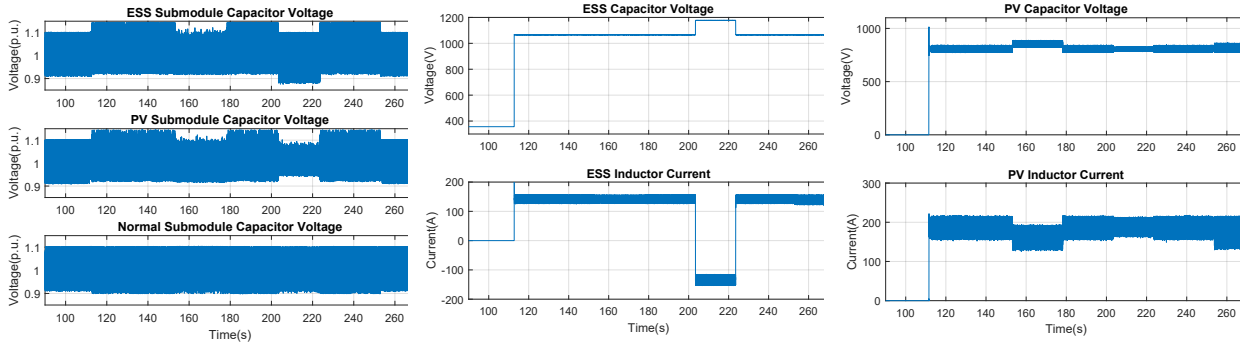

(a) (b) (c)

Figure 28. HIL test results to evaluate L2 control algorithms and communication from L2 controller to the MARS hardware: (a) capacitor voltages in each type of SM, (b) one ESS SM voltage/current, (c) one PV SM voltage/current.

Milestone M9.0 milestone, “Implementation of real-time PE-HIL algorithms, has been completed.

3.10 IMPLEMENT CONTROL ALGORITHMS IN PLATFORM AND VALIDATE

3.10.1 Implement the Multi-Level Multi-Rate Algorithms in the CPU

3.10.1.1 Implementation of Upper-Level L1 Control Algorithms in CPU

The upper-level L1 controller algorithms of MARS that include the VSG, ac-side current control, dc current control, and third-order harmonic voltage injection are implemented in the CPU (of the L1 control platform). The developed controller algorithms in the CPU are tested stand-alone with reduced-order MARS and ac power grid models developed in Task 2.

The tests are performed under various operating conditions of MARS with and without disturbances to ensure reliability of the model.

VSG Controller Tests in CPU

The real-time VSG frequency response of MARS for an 804.4 MW generation loss in WECC at $t = 5$ s is shown in Figure 29(a). The VSG in the L1 controller is responding to the change in frequency observed due to the loss of generation. The CPU use and the mean computation time of the upper-level L1 control algorithms are shown in Figure 29(b); 3.79% CPU is being used, and the mean computation time is 2.27 µs with no overruns for a control time step of 60 µs.

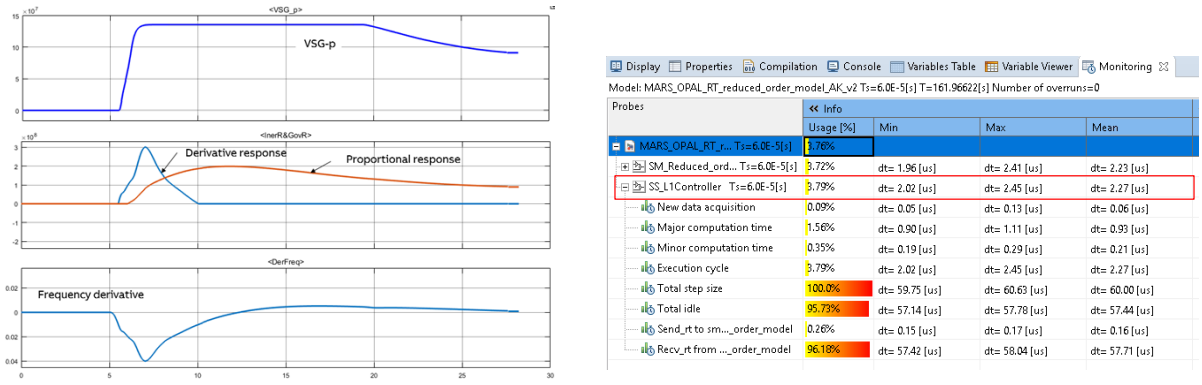

(a) (b)

Figure 29. (a) Real-time VSG frequency response for a generation loss 804.4 MW in WECC. (b) Opal-RT CPU use and computation time snapshot.

The dynamic available power capability in MARS under different operating conditions is shown in Figure 30(a). This limit is incorporated in the MARS control system. The robustness of the VSG controller is evaluated under different SCRs and system inertia. The gains used in the VSG controller had to be reduced in low SCR cases, with derivative response removed under very low SCR cases (that limit the inertial response). The successful provision of frequency support is shown in the figure. Similar tests have been performed during faults to evaluate the VSG response, and successful voltage support by MARS was observed.

Case #	MARS Dispatch	Reserve	WECC Inertia	Voltage Gain	SCR
1	Pref = 200MW, Pdc_ref = -200MW	135.8 MW	23	1.0	7
2	Pref = 200MW, Pdc_ref = -200MW	135.8 MW	23	1.0	4
3	Pref = 200MW, Pdc_ref = -200MW	135.8 MW	23	1.02	2
4	Pref = 200MW, Pdc_ref = -200MW	135.8 MW	23	1.07	1
5	Pref = 200MW, Pdc_ref = -97MW	32.8 MW	23	1.0	7
6	Pref = 200MW, Pdc_ref = -97MW	32.8 MW	23	1.02	2
7	Pref = 200MW, Pdc_ref = -200MW	135.8 MW	18	1.0	7
8	Pref = 200MW, Pdc_ref = -200MW	135.8 MW	18	1.02	2
9	Pref = 200MW, Pdc_ref = -200MW	135.8 MW	10	1.0	7
10	Pref = 200MW, Pdc_ref = -200MW	135.8 MW	10	1.02	2

Case #	System SCR	System Inertia	Reserved Capacity of MARS	VSG Performance	Improvement in Nadir (%)	Improvement in steady state (%)
1	7	23	135.8 MW	Stable, Fast response No oscillations	16.94	7.65
2	4	23	135.8 MW		17.43	7.64
3	2	23	135.8 MW		18.22	5.89
4	1	23	135.8 MW	Inertial response gain reduced	14.81	7.27
				Proportional response only	11.01	7.27
5	7	23	32.8 MW	Stable, Fast response No oscillations	4.58	7.44
6	2	23	32.8 MW		3.73	3.83
7	7	18	135.8 MW		19.29	8.40
8	2	18	135.8 MW		22.66	7.74
9	7	10	135.8 MW		25.49	8.54
10	2	10	135.8 MW		22.31	7.88

Figure 30. (a) Test cases for grid frequency support from MARS. (b) Grid frequency improvements with support of MARS.

EBC

The EBC criteria have been implemented to enable or disable the EBC in the L1 control of MARS. The EBC aims to provide energy balancing between different types of SMs (PV SMs, ESS SMs, and normal SMs), thus it can help maintain the capacitor voltages of different types of SMs within the predefined upper and lower voltage limits. However, not all operating conditions need the EBC to balance the system; in addition, the EBC will increase the system power losses by injecting the fundamental frequency circulating current. It is necessary to set the EBC criteria so that the system knows when to disable the EBC control. The EBC for MARS at Pittsburg will be enabled when the dc power is negative; or when ac power is less than 240 MW.

The EBC and circulating current controllers along with the EBC criteria are integrated in the CPU with the rest of the upper-level L1 controller algorithms. The L1 controller algorithms have been tested under different steady-state operating conditions, loss of generation, and faults. The reduced-order models of MARS and ac grid were used to evaluate the L1 controller algorithms in the CPU through real-time simulations. The test results were as expected and stable. The resource utilization in the CPU of the L1 controller is approximately 3.9%.

3.10.2 Implement the Low-Level Algorithms in the FPGA

The L2 control algorithm for the MARS was developed in the FPGA. The logical structure of the control algorithm was developed according to the design of the L2 controller. At the beginning, the algorithm reads the front-end half-bridge configuration and finishes the initialization. After receiving the "enable" signal from front-end half-bridge system, the algorithm starts operation. Firstly, the algorithm updates the required number of SMs that need to be operated, the value of delta[k] from L1 control algorithm in every 60 µs. It also updates the MARS arm current $I_{arm}[k]$, and SMs' capacitor voltage $V_{cap}[k]$ from front-end half-bridge system in every 4 µs. Secondly, the algorithm finds out one SM that has the maximum or minimum capacitor voltage. If the maximum voltage is larger than the user-specified upper voltage limit, the algorithm will turn on or off the corresponding SM based on the direction of the MARS arm current. Similarly, if the minimum voltage is smaller than the user-specified lower voltage limit, the corresponding SM will be turned on or off based on the direction of the MARS arm current. This process is used to avoid over-voltage and under-voltage on the SM capacitor. Lastly, the algorithm finds out the number of SMs to be executed in each MARS arm and turns them on or off depending on the direction of the MARS arm current. When the arm current is positive, if more SMs are needed, the SMs with lower capacitor voltage will be turned on to increase the voltage. If fewer SMs are needed, the SMs with higher

capacitor voltage will be turned off to decrease the voltage. A similar operation is done when the arm current is negative. This process balances the SM capacitors' voltage in each MARS arm. When finishing all these processes, the algorithm will go back to check the "enable" signal and repeat the whole process in every 4 µs. After the FPGA model development was finished, six L2 controllers were integrated to balance the SM capacitor voltages in six MARS arms. The real-time simulation results from MARS at Pittsburg, presented in Section 3.10.1, indicate that the L2 control algorithm worked as expected even under varying operating conditions.

3.10.2.1 L3 Controller:

L3 control algorithms for the PV and ESS SMs were developed in the FPGA of the MARS HIL platform. The FPGA development methodologies used in developing the L3 controller were similar to those used in the dc-dc converter model. Although the PV and ESS SMs send different inputs to the corresponding controllers, the structure of the controllers is the same with two proportional integral (PI) control loops. With pipelining, a single FPGA controller model instantiation has the calculation capability for 2,000 SMs running in a 100 µs time step. One L3 controller was placed in the FPGA to calculate the required number of PV SM inputs from six arms, and another L3 controller was placed to calculate all ESS SM inputs. The MARS HIL simulation model is summarized in Figure 25.

3.10.3 Implement the Lowest-Level Algorithms in One DSP

The L3 control algorithm has been implemented in the DSP using Code Composer Studio and evaluated in a single SM. The single SM test using the DSP provides updates to the gains that will maintain stable operation of MARS. As shown in Figure 31, the measured input voltage and inductor current will be sent from the sensors of the dc-dc converter and will be received by the DSP through an analog-to-digital converter pin. The gating signals generated by the DSP are routed to the dc-dc converter.

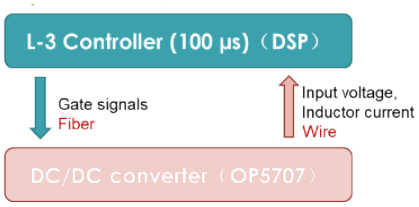

Figure 31. Interface board design for testing DSP L3 controller algorithm.

To test a single L3 controller in the DSP, a bidirectional dc-dc converter model was built in the FPGA of the real-time simulator. The outputs of the real-time simulator that are sent to the DSP are the ESS-side voltage, inductor current, and the front-end half bridge capacitor voltage. The gating signal is generated from the DSP board and sent to the real-time simulator. The results for one test case for the closed loop control are provided in Figure 32. Several other operating conditions were tested for robustness (P_{essref}= 195 MW for individual ESS SMs).

As can be seen from Figure 32, the current is tracking its expected reference (= $P_{ess,ref}/V_{ess} = P_{ess,ref}/1{,}000$), and the power is tracking its reference. The HIL tests are used to fine-tune the gains in the L3 controllers.

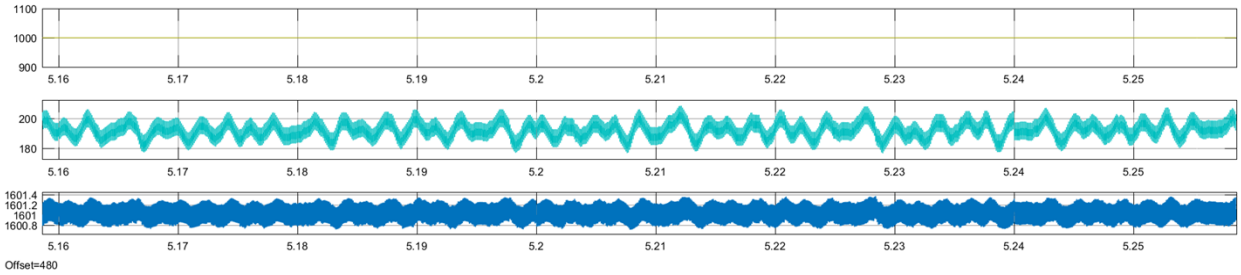

Figure 32. The ESS side voltage (V), the inductor current (A), and the front-end half bridge capacitor voltage (V).

3.10.4 Update the Business Model for the MARS Plant

The business model for MARS has been updated from Task-4 (Section 3.4) to (1) identify costs of isolated MARS with isolated PV-SMs and (2) incorporate value of ancillary services like fast frequency response (inertial, primary frequency); regulations; and spinning reserves. A cost reduction of up to 40% in electrical costs was identified in MARS as compared to baseline case upon cost upgrades. A reduction in levelized costs by up to $6/MWh is expected from the ancillary services provided by MARS based on market research and literature on existing markets. Further benefits from ac-dc systems use in addition to providing stability services (e.g., continuity of operation under faults without momentary cessation, reactive power support) have been identified but not quantified in the ancillary benefits. The use of ac-dc systems, instead of only ac systems, can provide up to ~14% in additional benefits.

Milestone M10.0, “Implement control algorithms in platform and evaluate. Updated business model presented,” has been completed.

3.11 DESIGN AND DEVELOP CYBER HARDWARE IN LOWER-LEVEL CONTROLLERS AND IMPLEMENT CYBER-SECURE SOLUTIONS IN HIGHER-LEVEL CONTROLLER

3.11.1 Design a Cyber Protection System

The cyber intrusion detection system is implemented at the upper and lower levels of the L1 controller to detect bad data or commands. It is shown in Figure 33. The algorithms are implemented as a layer in the CPU to evaluate the signals received and sent from the L1 and L2 controllers. They are based on estimation of the next time-step states from measured states and internally generated MARS commands (e.g., modulation signal) and comparison with the next time step measured signal to identify vulnerabilities and feasibility of the operating condition.

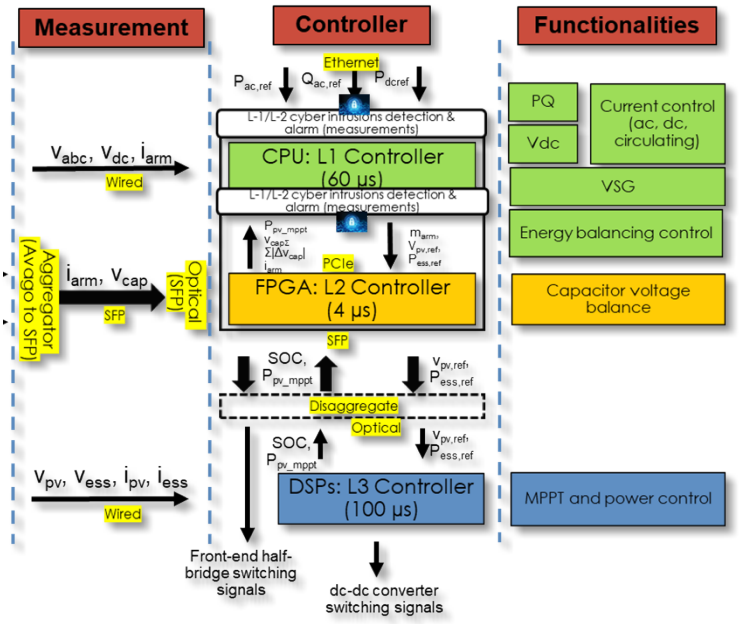

Figure 33. Cyber protection system embedded within the MARS control system.

For example, the protection algorithms for the malicious power order commands that have been proposed are summarized in Figure 34. To secure MARS from executing power order commands that may cause overloading of the local grid, the MARS L1 controller will continuously monitor and estimate its power output to the local grid or identified ac line power flow resulting from the power order change command. It will stop the full execution of the power order change and alarm the MARS control house and the system operator if the power injection to the local grid exceeds a predefined operational security constraint or if the identified ac line power flow exceeds line protection trip threshold. To secure the MARS L1 controller from manipulated measurements, the MARS L1 controller will continuously perform consistence assessments of measurements. It will block execution of the emergency power control such as frequency response or dynamic voltage support resulting from manipulated measurements and alarm the MARS control house for the identified measurement issues. The high-level L1 control's VSG secure MARS measurement is described in Appendix A.4.1. The lower-level L1 control's intrusion detection is based on artificial intelligence (AI) algorithms that estimate the expected measurement and compare it with the measurement to identify intrusions.

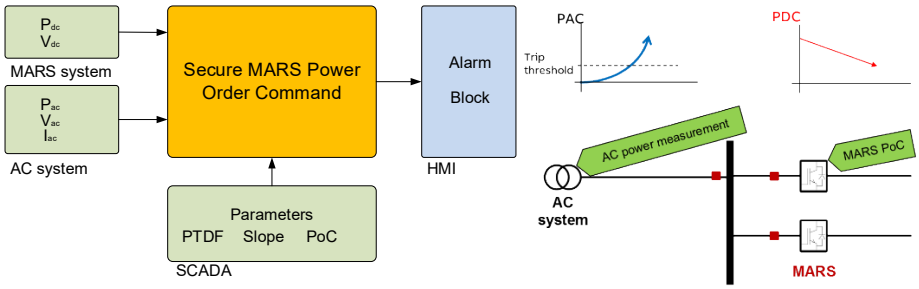

Figure 34. Cyber security protection for potentially malicious power order commands.

3.11.2 Integrate Sensor and Communication Hardware with Designed Embedded and Computational Platform for Cyber-Security

3.11.2.1 Upper-level L1 control's measured data protection

Based on the algorithm described in the previous sub-task, additional power measurement and voltage measurement may be needed.

3.11.2.2 Lower-level L1 control's measured data protection

A defined training data set based on different operating conditions of MARS is used to train the different AI algorithms that include (1) a nonlinear autoregressive network with exogenous inputs (NARX), (2) a decision tree, and (3) a spiking neural network (SNN). While NARX can be implemented within the existing control system, the decision tree and the SNN were evaluated for implementation on a neuromorphic computing unit. The training has been completed for the data-driven prediction of the states in MARS in the lower-level L1 control system (arm currents and capacitor voltages). The data-driven prediction is compared with the corresponding measured state to detect falsified data injection (or bad data). A comparison between the different algorithms is performed on the training duration required and the size of the network generated. While the training of the SNN algorithm takes several days based on the data set using a scalable high-performance computer, the NARX takes minutes to train on a general-purpose desktop computer. The training of decision tree is fast (within 1 s). The size of the SNN is 818 neurons and 1,180 synapses. The depth of the decision tree is 12. The size of the NARX is 13 neurons and 30 synapses. The training accuracy obtained in the SNN, the decision tree, and NARX are 79.42%, 91.31%, and >99%, respectively. Based on this evaluation, NARX was chosen to make predictions due to its higher accuracy. This algorithm does not require additional sensor, communication, or computing hardware for the lower-level L1 control system.

3.11.3 Implement and Test the Cyber-Secure Features

3.11.3.1 Upper-level L1 protection

In order The secure MARS power order command (secure MARS cmd) function, which has been developed to detect the malicious power order commands to the MARS system, consists of three methods: offline secure MARS cmd – ac overload, online secure MARS cmd – ac overload, and offline secure MARS cmd–capability limit violation. The three methods are summarized below:

- Method 1: Prevent MARS operational limit violation (capability limit violation):

$$P_{\text{MARS\_min}} \leq \ -P_{\text{dc}_{\text{ref}}}(t) + P_{\text{ac}_{\text{ref}}}(t) \leq P_{\text{MARS}_{\text{max}}}$$

Method 2: **Prevent ac** overloading using power transfer distribution factors (PTDFs) (offline secure MARS **cmd – ac** overload):

$$P_{\text{line}}(t_{\text{final}}) = P_{\text{line}}\,(t_{\text{init}}) + P_{\text{ac\_ref}} \times PTDF$$

Method 3: **Predict ac o**verloading based on incremental rate of flow change (online secure MARS cmd – **ac** overload):

$$P_{\text{line}}\,(t_{\text{final}}) = P_{\text{line}}(t_k) + m_{\text{AC}} \times t_{\text{RAMP}}$$

where $P_{\text{line}}(t_k)$, represents the line flow at t_k, m_{AC} is a slope of flow change, and t_{RAMP} is the remaining ramping time. The command will be blocked if potential problem is detected by method 1 or method 2. The execution of command will be terminated if potential problem is detected by method 3.

One of the simulation results to block ac overload is shown in Figure 35, which shows successful detection of ac line overload through both offline and online secure MARS cmd.

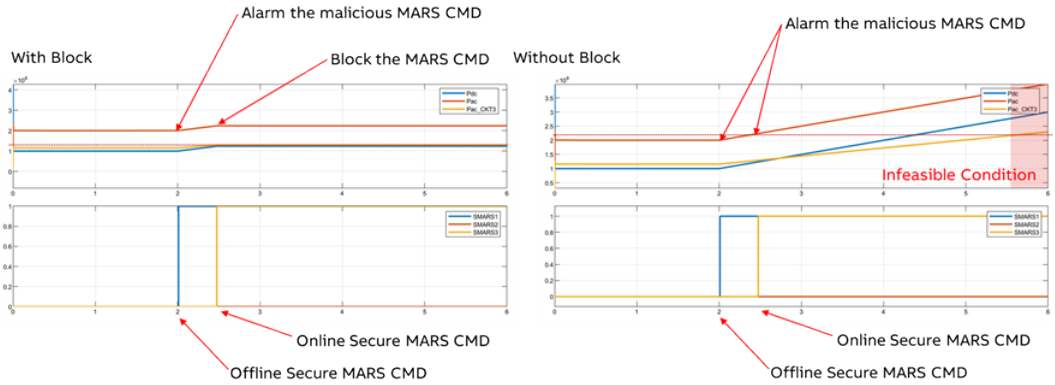

Figure 35. Test case for detection of ac line overloading issues (left: with block upon intrusion detection to avoid infeasible operating condition; right: without block that leads to infeasible operating condition).

3.11.3.2 Lower-level L1 protection

The NARX-based algorithms used to estimate signals have been tested under different operating conditions (normal and abnormal). The operating conditions include various commanded ac-side power, dc-side power, PV power, ESS power, ac-side faults, and loss of generators. Based on the AI-based estimation algorithms (that use NARX), the next time-step arm currents are estimated from internal MARS commands (modulation indices) and measured arm currents. The different operating conditions tested indicated that estimated data closely follows the measured data. These estimated signals (arm currents and capacitor voltages) are compared in the next time step with measured signals to detect FDIA or bad data on measured signals. An example simulation test result is shown in Figure 36, where bad data are detected in arm currents.

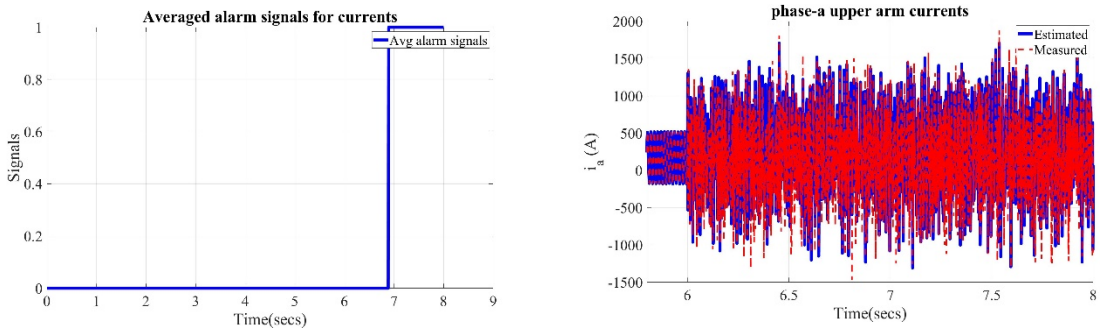

Figure 36. Alarm and current estimates when FDIA happens on current measurements.

The go or no-go decision point M 11.0 G/NG-5, "Develop cyber hardware in lower-level controllers and implement cyber-secure solutions in higher-level controller," has been completed.

3.12 DEVELOP PE MODULE

3.12.1 Assemble Gate Drivers, Sensors, and Communication Hardware in the PE Module. Test and Evaluate

3.12.1.1 ESS SM

The interface board, designed in Task-6 and shown in Figure 37, has been soldered and evaluated. All power supply and signal transmission functions work normally. The performance of the gate drivers was evaluated, and latencies were measured. The latency of the gate driver for an SiC Metal-Oxide-Semiconductor Field-Effect Transistor MOSFET module shown in Figure 38 has been tested. The delay of rise edge between its input and output signals is 296 ns; the delay of fall edge is 144 ns. The latency between the outputs of two gate drivers (driving two series connected SiC MOSFETs) has been measured and is within 4 ns, indicating that the two MOSFETs have almost synchronized actions. The performance of the gate drivers is adequate for the 10 kHz switching frequency to be used (100 µs time period). The gate resistor was chosen for the optimum rise time and fall time (i.e., times that do not lead to voltage overshoots during switching on or off.

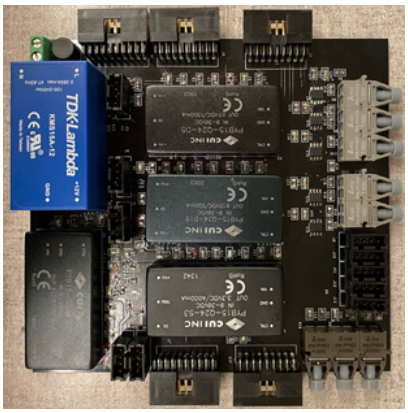

Figure 37. Interface board.

(a) (b)

Figure 38. Time delay between the input and output signals of gate driver (a) rise edge, and (b) fall edge.

3.12.2 Assemble Semiconductor Devices and Heat Sinks into the PE Module

3.12.2.1 ESS SMs

The costs of the ESS SMs in MARS at Pittsburg and Victorville have been updated based on updates to the inductor costs. The ESS SMs in MARS at Pittsburg and Victorville, shown as 3D diagrams in Figure 39, were updated to minimize parasitics.

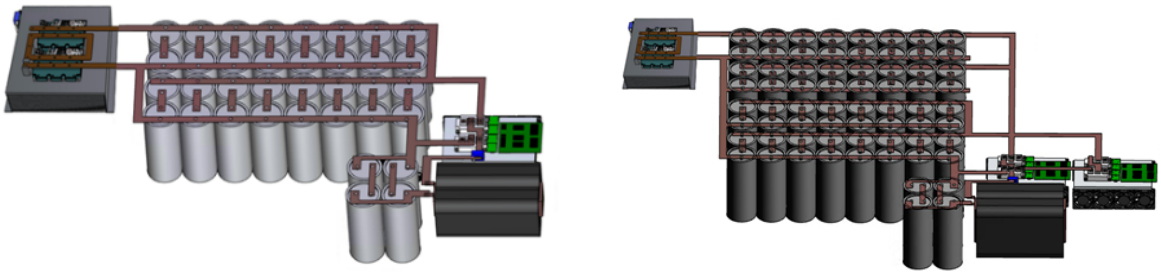

(a) (b)

Figure 39. 3D model of the ESS SMs in MARS at (a) Pittsburg and (b) Victorville.

3.12.2.2 PV SMs

The semiconductor devices, transformers, inductors, capacitors, heat sinks, gate drivers, fans, voltage sensor, current sensor, interface board, and other components were identified for the PV SMs. Based on the components identified, the costs of PV SMs in MARS at Pittsburg and Victorville were calculated, and their efficiencies were estimated.

3.12.3 Perform Double-Pulse and Low-Power Test of PE Module

3.12.3.1 ESS SMs

The double-pulse test is performed on switches with dc bus voltage being 800 V. The test result is shown in Figure 40; the test setup is shown in Figure 41. The turn-on energy in this case is 1.6 mJ; the turn-off energy is 0.37 mJ. The turn-on time is 354 ns; the turn-off time is 664 ns. No transient overshoot voltage was observed because a buffering capacitor compensates for the parasitics.

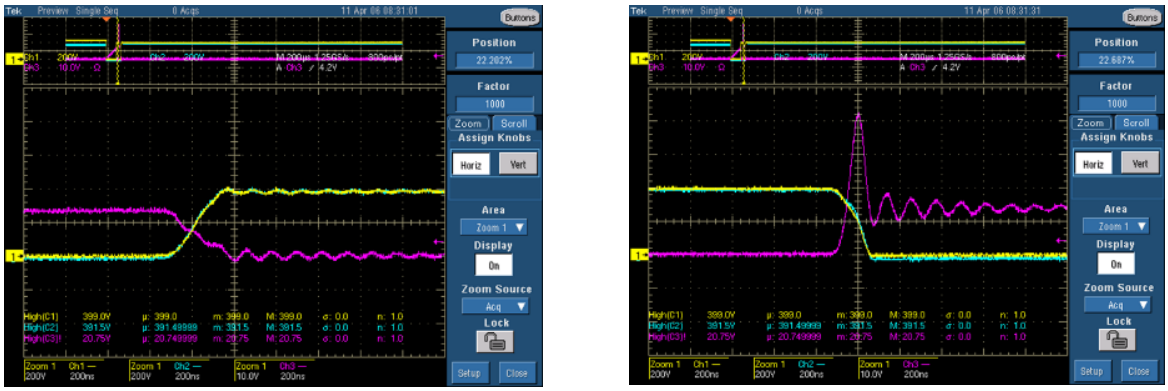

(a) (b)

Figure 40. Double-pulse test for switches (a) turn off transient, and (b) turn on transient. CH1: v_{ds1}, CH2: v_{ds2}, CH3: i_{ds}.

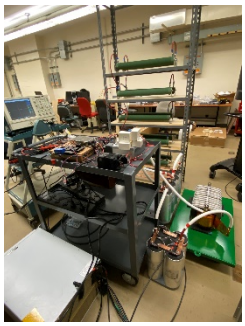

Figure 41. The test setup.

The double-pulse test results are used to estimate the parameters used in the theoretical calculations (e.g., turn-on energy, turn-off energy). The results are compared with a datasheet. Next, low-power tests are performed on the ESS SM dc converters. Based on the low-power tests under different operating conditions, the efficiency of operation from experimental test results are compared with the theoretical calculations. The calculations are very close to the experimental results and the errors are less than 1%. Based on the calculations, the efficiency of the ESS SM's dc-dc converter is expected to be greater than 99% in most operating conditions in MARS at Pittsburg. The same calculation was performed for MARS at Victorville, and the efficiency was found to be greater than 98.6% in most operating conditions.

The go or no-go decision point M 11.0 G/NG-6, "Developed PE module," has been completed.

3.13 DEVELOP AC SYSTEM MODELS IN REAL-TIME SYSTEM

3.13.1 Implement AC System Dynamic Models in Transient Real-Time Simulation

The real-time simulation model of ac grid has been developed in a single core of the CPU based on the offline EMT ac grid simulation model developed in Task 1. The model has been evaluated and compared with the offline model. The normalized root-mean-square (RMS) errors between PSCAD (offline) and real-time simulation results are shown in Table 7 under different operating conditions. The errors were observed to be less than 5%. Additionally, no overruns were observed with the ac grid model implemented in one core of the CPU.

Table 7. Normalized RMS error between PSCAD and real-time simulation results [a]

Case	Calculation period (s)	Voltage (%)	Current (%)	Active power (%)	Reactive power (%)	Frequency (%)
Flat run	10–30	< 0.01	< 0.01	0.01	0.11	< 0.01
Under-frequency event at 10 s	10–50	< 0.01	0.05	0.02	0.40	< 0.01
Apply 3P-G fault at 10 s	9.9–10.1	0.23	0.44	0.21	0.71	0.40
Clear 3P-G fault at 10.25 s	10.15–10.35	1.51	0.88	1.31	4.20	0.36
Apply L-L fault at 20 s	19.9–20.1	0.22	0.18	0.23	3.42	0.08
Clear L-L fault at 20.25 s	20.15–20.35	1.13	0.24	0.39	4.86	0.08

[a] The normalized error of voltage and current is the maximum error in three phases.

Milestone M 13.0, "Develop ac system models in real-time system," has been completed.

3.14 IMPLEMENT CYBER SECURITY ALGORITHMS AND EVALUATE IN MARS

3.14.1 Implement Secure Communication Algorithms in Developed Control System

In the hierarchical control platform of MARS, the upper-level cyber security algorithms are implemented in the CPU of the control platform to ensure secure communication of command and data. The algorithms are described under Task 10. The implemented algorithms in the upper-level L1 are tested individually. One of the test results is shown in Figure 42. The precondition to power order command change in Figure 42 is unviable because the new power order command change results in an ESS power rating violation. In the figure, the violation is detected, and the change of power is blocked (in the case with CMDBlock enabled). The comparison with and without the block of the power command is shown in the figure (right vs. left). The implemented algorithms have been tested under ac network overloading, malicious ramp rate, and normal operating conditions to evaluate the implemented algorithms individually. Based on the tests, the algorithms have shown detection in all use cases.

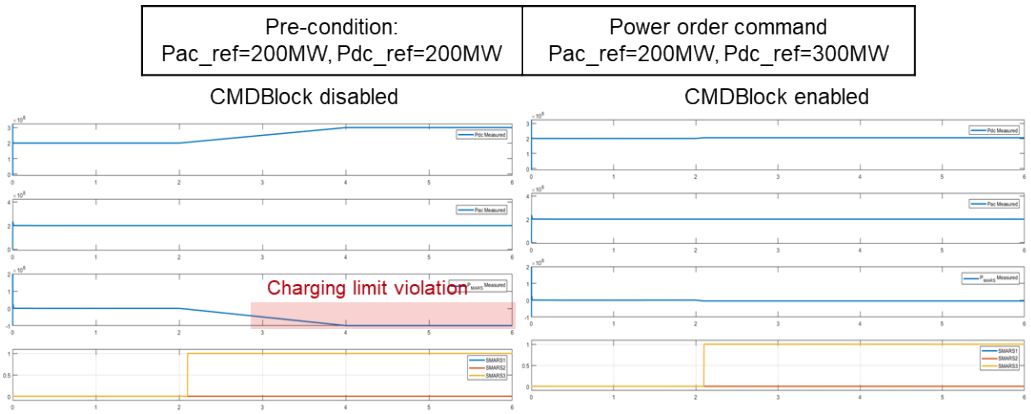

Figure 42. Test case for malicious CMD that may cause ac network overloading.

3.14.2 Implement Cyber-Attack Detection Algorithms

The lower-level L1 control's measured data protection has been implemented in the L1 controller developed in the CPU of the control platform. The protection features include estimation of the measured data using the NARX AI model and comparison with measured data averaged over a predefined period of time to detect anomalies. Stand-alone tests have been performed to indicate real-time and error-free operations capability. An example for alarm signal generation when intrusion happens is shown in Figure 43, which shows successful detection of bad data in arm currents.

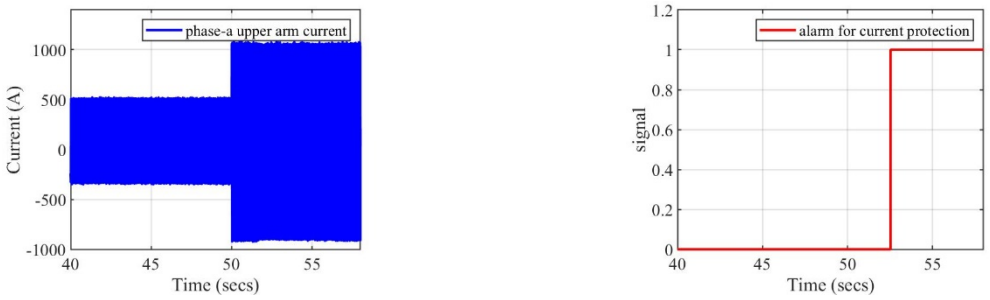

(a) (b)

Figure 43. Example for alarm signal generation: (a) iarm current and; (b) alarm for current protection.

Milestone M-14.0, “Implement cyber-security algorithms in MARS and evaluate,” has been completed.

3.15 COMPLETE MARS SYSTEM INTEGRATION AND EVALUATE PERFORMANCE

3.15.1 Integrate PE Module with HIL Platform and Test

3.15.1.1 ESS SMs

The ESS dc-dc converter has been tested under additional voltage and power levels. The tests mimic the operation of the dc-dc converter based on the HIL implementation. The test results were recorded, and the measured efficiencies were compared with calculations (similar to the tests completed in Task 12). The efficiencies measured in experiments were close to the theoretical values (with less than 1% errors), which validates the efficiency calculations used for SMs in overall efficiency calculation for MARS.

3.15.1.2 PV SMs

The 3D diagrams of the PV SMs’ DC-DC converters in MARS at Pittsburg and Victorville are shown in Figure 44. The design is intended to minimize parasitics. Low-power tests were performed on the PV SM’s dc-dc converter in MARS at Pittsburg based on the operation observed in HIL tests and simulations. The test setup is shown in Figure 45. The experimental results from the low-power tests were compared with the theoretical efficiency calculations. The comparison showed that the calculations were very close to the results, with errors less than 2.6%.

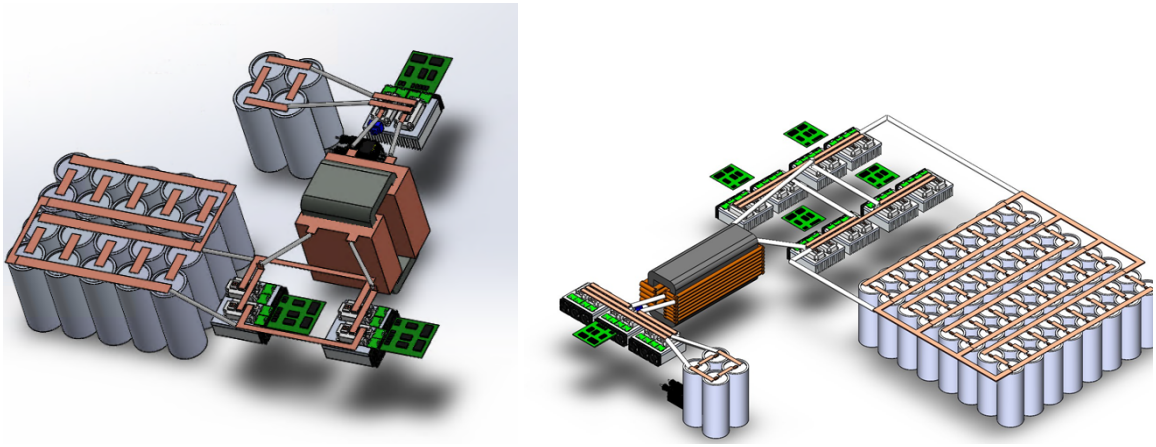

Figure 44. The 3D models of the isolated PV SM’s dc-dc converters: (left) Pittsburg, (right) Victorville.

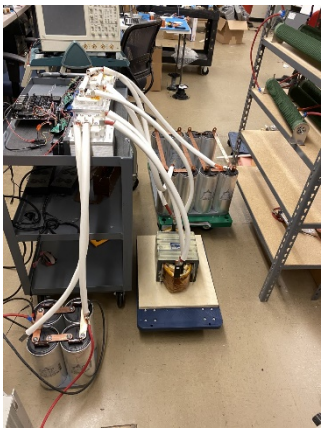

Figure 45. The experimental prototype of the isolated PV dc-dc converter for MARS at Pittsburg.

3.15.2 Integrate PE-HIL with AC System Real-Time Simulation and Test

Upon the integration of the ac power grid's model with the MARS model in the real-time simulation model, different tests are performed for faults and loss-of-generation events. In these tests, the control platform (L1-L2) of MARS was connected to the MARS HIL platform. The results of grid and within MARS measurements, as shown in Figure 46 and Figure 47, indicate that the integration was successful because the results are as expected (i.e., with the active power tracking its reference, the voltages are at the expected values).

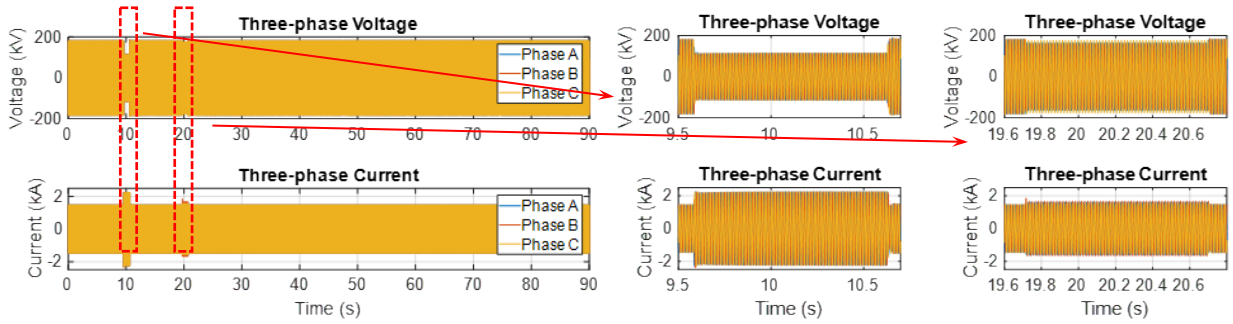

(a) (b) (c)

Figure 46. (a) Real-time simulation results of voltages and currents at the connection point of MARS, (b) zoomed-in waveforms during 3P-G fault, and (c) zoomed-in waveforms during L-L fault.

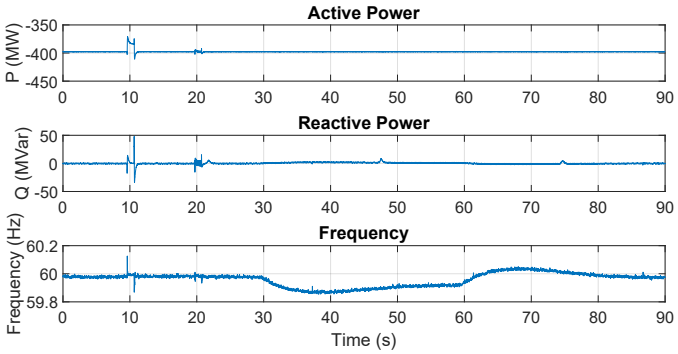

Figure 47. Real-time simulation results of active power, reactive power, and frequency at the MARS connection point.

The results of the HIL testing of MARS, as shown in Figure 48, demonstrate that the capacitor voltages for each type of SM were balanced, showcasing the successful operation of the L2 controller. The L1 controller algorithms for MARS are not integrated in this case.

The maximum delay between the ac grid real-time simulation and the MARS real-time HIL has been identified to be one time-step (60 µs), which provides low latency integration. The successful test results indicate synchronization between ac grid and the real-time MARS simulations.

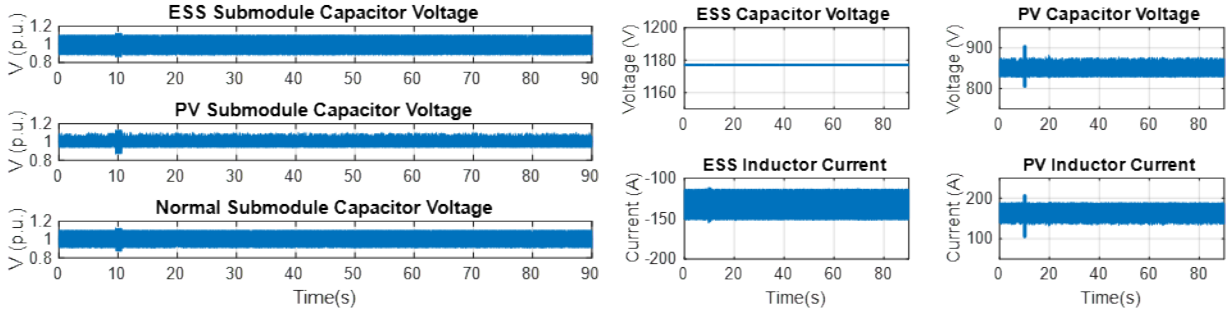

(a) (b)

Figure 48. (a) Capacitor voltages in representative submodules, (b) one ESS and PV SM outputs.

Milestone M 15.2, "Integrate PE-HIL with ac system real-time simulation and test," has been completed.

3.15.3 Integrate Control System in MARS and Test under Various Conditions

The hierarchical control platform (L1-L2) in MARS with both L1 and L2 controller algorithms (without the cyber intrusion detection algorithms) has been evaluated in HIL testing with updated gains to ensure stable operation. The HIL setup us shown in Figure 49. To integrate the L1 controller algorithms with the rest of the setup from Section 3.15.2, each individual algorithm was incorporated and tested to update gains from the previous stand-alone tests for only-L1 controller. Once the gains were fine-tuned, the hierarchical (L1-L2) control platform of MARS was evaluated in HIL under different operating conditions as well as grid events. One example event and the corresponding support provided by the VSG control algorithms in MARS is shown in Figure 50. As shown in the figure, MARS is able to improve frequency response by up to 16%. through VSG support, The response of MARS during a three-phase fault is shown in Figure 51. As shown in the figure, MARS is able to provide continuity of operation with or without VSG control. With VSG control, MARS is able to provide additional reactive current to support the grid. The operation of MARS was observed to be stable under all the tests performed, showcasing the success of the harmonized control methods in the hierarchical control platform of MARS. It has been shown to provide up to 16% improvement in frequency response and 100% disturbance rejection in all the fault cases tested.

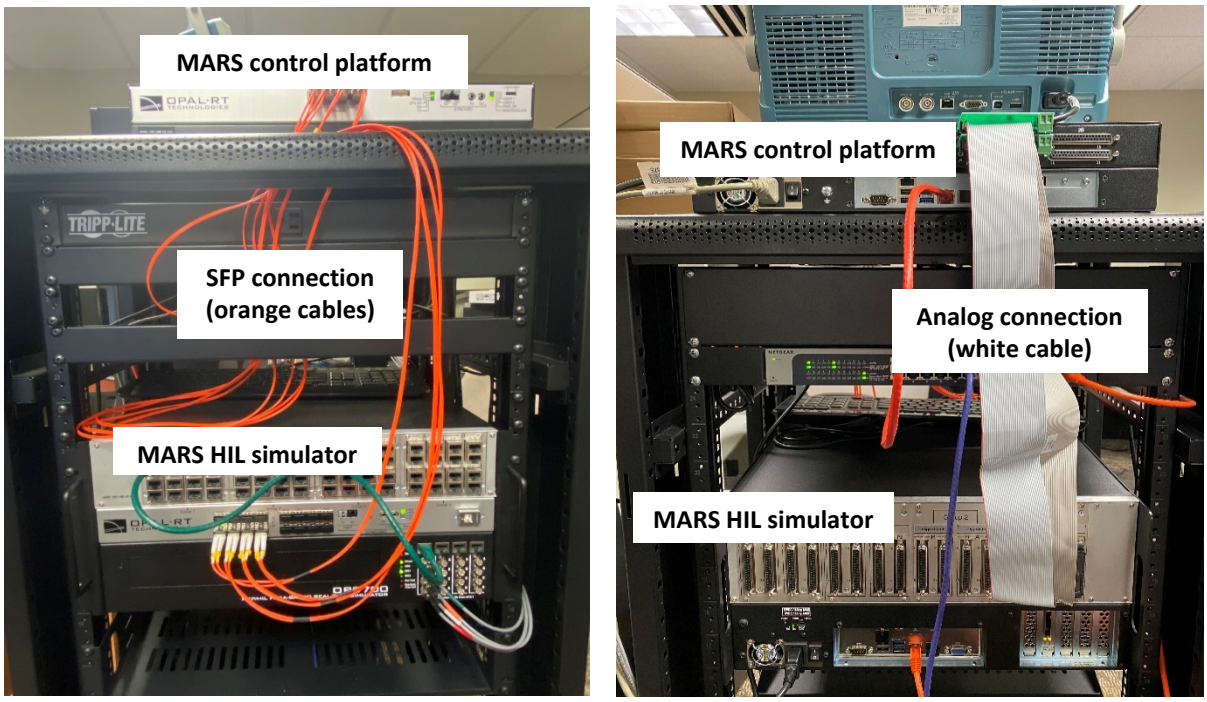

Figure 49. HIL setup of MARS: (left) front-side connection; (right) back-side connection.

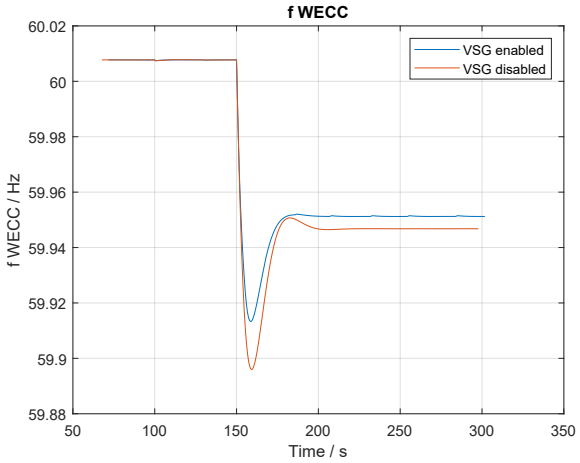

Figure 50. Frequency measured in WECC grid with loss of generation (with and without MARS' VSG support).

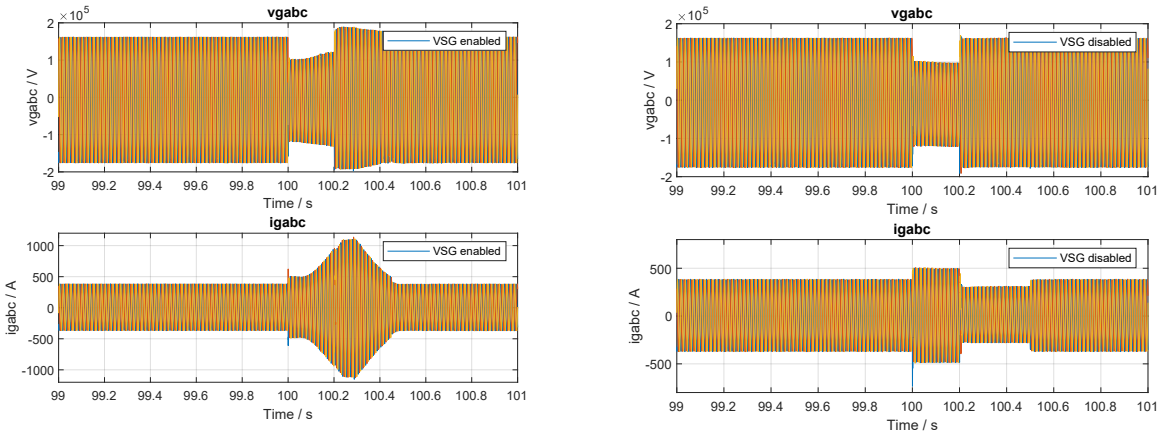

(a) (b)

Figure 51. (a) Grid-side three-phase voltage and current with VSG controller enabled. (b) Grid-side three-phase voltage and current with VSG controller disabled.

Milestone M 15.3, "Integrate control system into MARS & test under various operating conditions," has been completed.

3.15.4 Integrate Cyber-Security System and Test under Various Attacks

The cyber intrusion detection algorithms have been integrated in the hierarchical (L1-L2) control platform of MARS.

3.15.4.1 Lower-level L1 cyber algorithms integration and testing in HIL

Tests have been performed under various normal operating conditions and under false data injection (FDI) to measured data (e.g., arm currents, capacitor voltages). Various types of FDIs (e.g., data rotation, DC addition, AC addition) have been initiated on the measured data. The normal operating conditions under which MARS was tested include Pac = Pdc = 300 MW, $P_{ac} = P_{dc}$ = 100 MW, $P_{ac} = P_{dc}$ = -100 MW, $P_{ac} = P_{dc}$ = -230 MW, P_{ac} = -50e6 MW, and P_{dc} = -74e6 MW. Stable operation of MARS and the performance of the L1 cyber algorithms were evaluated in these tests. Under normal operating conditions, the MARS system is stable and the alarm from intrusion detection remains turned off. Under all the FDIs, alarm from the intrusion detection algorithm in lower-level L1 in MARS turns on, indicating success in detecting bad data (or an FDI) in measured data. The example shown in Figure 52 showcases the successful detection of bad data within 3 s.

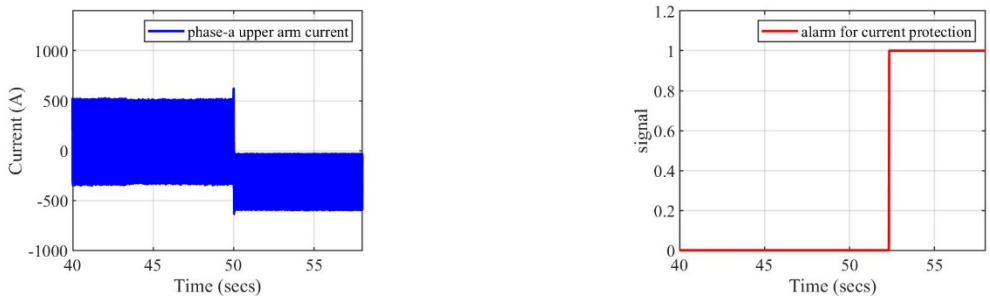

(a) (b)

Figure 52. FDI tests for $P_{ac} = P_{dc} = 100$: (a) arm current, (b) alarm signal.

3.15.4.2 Upper-level L1 cyber algorithms integration and testing in HIL

The following two test cases were identified for testing the upgraded control platform of MARS:

- test case for normal operating condition $P_{ac\_ref} = 200$ MW and $P_{dc\_ref} = 200$ MW
- test case of abnormal operating condition that may cause MARS operational violation with $P_{ac\_ref} = 350$ MW and $P_{dc\_ref} = 200$ MW.

The results for normal and abnormal operating conditions (without block and with block, respectively) are shown in Figure 53. During normal operating conditions the power command provided for the MARS system from SecureCMD block follows the ac dispatch power command, and the SecMARS3 (alarm) command for MARS operational violation is off. In the case of abnormal operating conditions, the power from the SecureCMD block is limited to the value at the instant where the SecMARS3 command is on. From these tests, one can deduce that the intrusions have been identified by the upper-level cyber algorithms and successfully blocked.

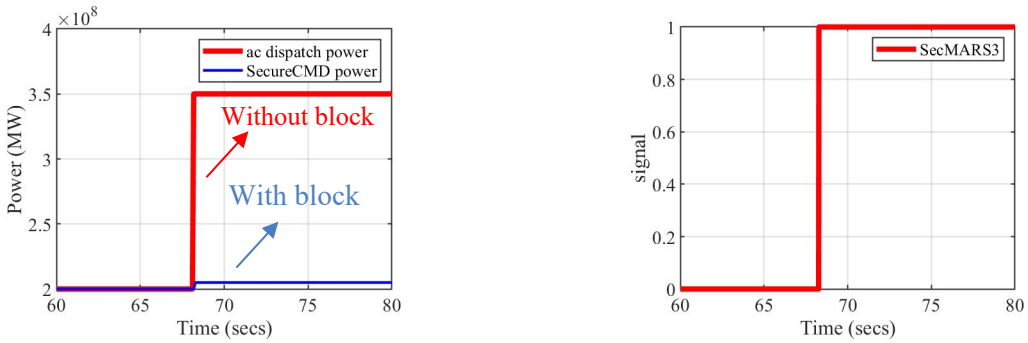

(a) (b)

Figure 53. Test case for abnormal operating conditions: (a) ac dispatch power and SecureCMD power and (b) SecMARS3 command for MARS operational violation.

Based on the tests completed under various normal, abnormal, and FDI cases, one can conclude that the use case–defined intrusions were detected with 100% success and without false detections during normal operations.

Milestone M 15.4, "Integrate cyber-security system and test under operating conditions, has been completed.

3.15.5 Evaluate Performance of the Completely Integrated MARS System

With all algorithms incorporated, comprehensive HIL tests were performed to evaluate the frequency and voltage support provision by MARS without triggering the cyber-security alarms. Various normal operating conditions and grid events were evaluated, and under all these operating conditions, the alarms from the cyber-security algorithms were not triggered. One of the test results when a loss of generation event and MARS provides support is shown in Figure 54. With MARS VSG support, up to 16% improvement in frequency response was observed (as compared to no VSG support) without triggering the alarm. This test is performed under four different operating conditions. Similarly, fault tests (both line-line and three-phase) were also performed at four different operating conditions, and no spurious trigger of alarm was observed while MARS provides continuity of operation. Different lower-level cyber-attacks under different operating conditions were evaluated and showed successful detection of intrusions in either arm currents or capacitor voltages: ac addition, dc addition, and data rotation. Detection of different upper-level cyber-attacks were evaluated and showed successful detection of intrusions in capability limits violation as well as ramp rate violations.

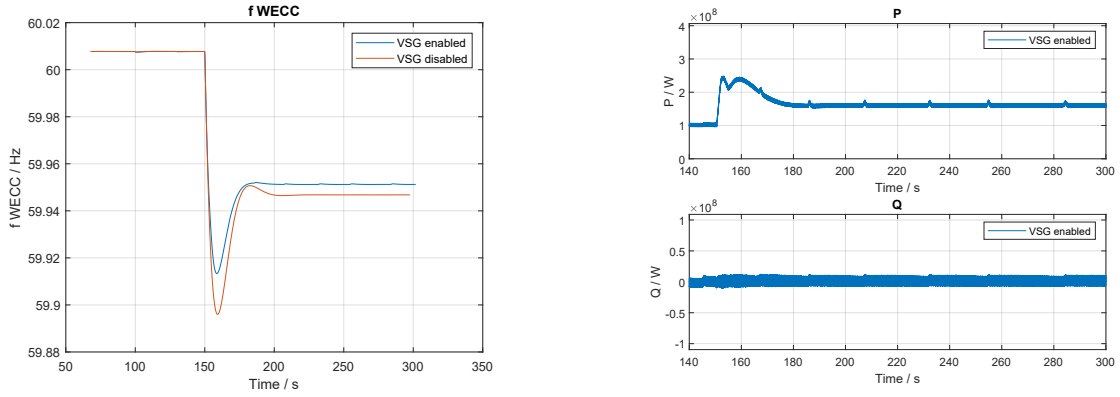

(a) (b)

Figure 54. Loss of generation at P_{ac} = 100 MW and P_{dc} = 100 MW: (a) Frequency measured with VSG enabled and disabled. (b) Active and reactive powers measured at grid side when VSG controller is enabled.

Milestone M 15.5, "Evaluate performance of the completely integrated MARS system," has been completed.

3.16 IDENTIFY VALUE PROPOSITION AND DEVELOP BUSINESS MODEL FOR COMMERCIALIZATION BASED ON PERFORMANCE METRICS, AND HIL DEMONSTRATION

3.16.1 Based on HIL Demonstrations, Quantify and Validate Performance

3.16.1.1 Upgraded state-of-the-art PV and hybrid PV+ESS plants

The discrete hybrid PV plant without upgrades could not provide continuity of operation during balanced and unbalanced transmission line faults for the same operating conditions and ac grid conditions as in the MARS system when connecting to a low SCR and low inertia grid. The main reason for such behavior is insufficient short circuit strength in the ac grid that led to unstable operation of the discrete hybrid PV plant.

Additional reinforcements such as synchronous condensers, shunt capacitors, and dampers were installed in the system to ensure enhanced stability. The synchronous condensers improved the short-circuit strength of the system and enhanced the stability of the connected plant. Shunt capacitors and dampers were also installed in the system to reduce the harmonics produced by the PV and ESS plant inverters. These upgrades, as discussed Task 4, are very expensive; an alternative solution of using HVdc links may be more cost-effective on a case-by-case basis.

3.16.1.2 Distribution grid–connected MARS

The system design and control concepts of MARS can be extended for distribution applications. Distribution Grid–Connected MARS (D-MARS). In general, a D-MARS plant could be interconnected to a distribution substation through medium-voltage dc (MVdc) link or tapped onto a MVdc intertie. Another promising use case is D-MARS enhanced MVdc intertie in distribution network.

The basic design of D-MARS at Pittsburg was considered for analysis. It is shown in Figure 55. The PV generation and energy storage dispatch profiles of D-MARS are based on the profiles of MARS at Pittsburg. The electrical system costs and the total system costs are estimated along with potential capital cost savings, efficiency improvement, and total LCOE and are compared with the values for the baseline design. The electrical costs can be reduced by up to ~20% in D-MARS as compared to a discrete development.

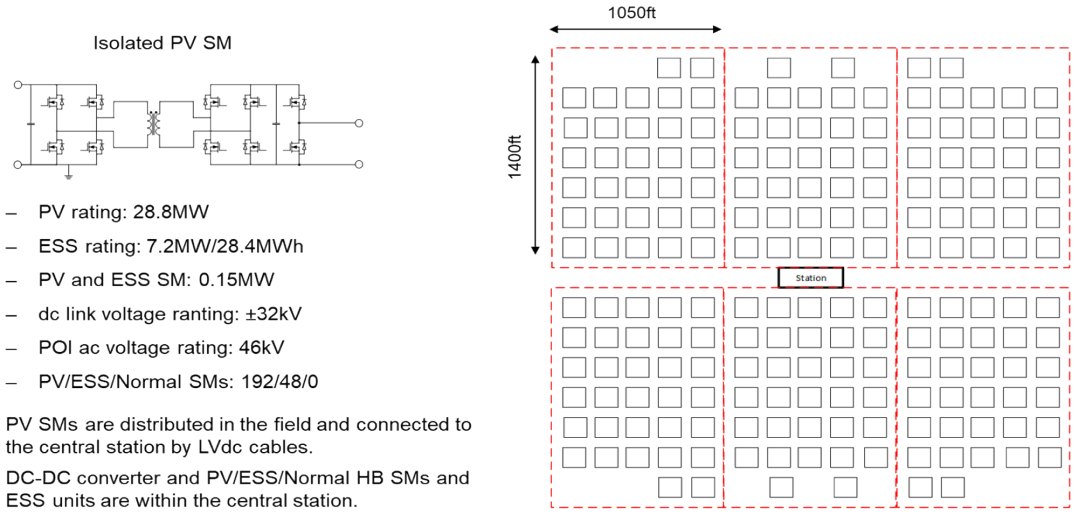

Figure 55. Basic design considerations of D-MARS.

3.16.1.3 Ancillary benefits from D-MARS

The estimated ancillary benefits for MARS at Pittsburg were applied to the Pittsburg D-MARS. That is, the system LCOE could be reduced by up to $3.60/MWh with inclusion of ancillary services offset from regulation, spinning reserve, and primary frequency response. Further LCOE reduction of up to $4.29/MWh could be expected from grid voltage support services. In total, the system LCOE could be reduced by up to $7.90/MWh from existing and near future ancillary markets. The total LCOE reduction is ~27%. LCOE may be reduced further through provision of inertial support.

3.16.1.4 Benefits from network capacity and resiliency enhancement from D-MARS

Additional benefits of D-MARS include enhanced load serving capacity and fast service restoration after an outage.

3.16.2 Finalize the Business Models for Commercialization of the Proposed Technology Business Models

The value proposition studies for MARS have shown a reduction in levelized costs on the order of 25% with inclusion of ancillary services such as dynamic voltage support, fast frequency response, frequency regulation, and spinning reserves. Further reduction is feasible through inertial services and improved utilization of ac-dc networks, among others. A MARS-type solution can integrate into existing HVdc links and/or future HVdc links/grid by tapping into an HVdc link with a voltage-source converter (VSC) or line commuted converter (LCC) substations, connecting to a VSC HVdc substation, and use as an intermediate terminal of an HVdc grid. In this project, MARS has been evaluated as a stand-alone technology to identify technical and economic benefits. The next steps, after the project, will be to identify the feasibility of integrating MARS into different future power grid scenarios (e.g., connectivity to existing LCC-based HVdc links, multiterminal dc with VSC and MARS).

3.16.2.1 Commercialization of MARS technology—pathway forward

By the end of this project, control architecture and algorithms and cyber intrusion detection algorithms were evaluated in HIL. Over the next 4 years, identification of MARS in different future power grid scenarios with system integration value will be showcased and protection system requirements will be

quantified. During the same duration, demonstration of D-MARS at a reduced scale will be conducted in a laboratory, and over the following 4 years, D-MARS will undergo a field trial. In the final 5 years, the field trial of MARS connected to a transmission grid will be completed and manufacturability of components in MARS can be established.

Milestone M 16.0, “Develop business model for commercialization based on performance metrics,” has been completed.

3.17 STANDARD COMPLIANCE OF MARS

3.17.1 IEEE 1547-2018 Compliance for Voltage, Frequency Support under Defined Disturbances

3.17.1.1 IEEE 1547-2018/PRC-024-3 compliance for frequency support for loss of generation

Twelve different frequencies have been applied at the MARS terminal of to evaluate the operation of MARS on the off-nominal frequency capability identified in NERC PRC-024-3 in western interconnection [57]. Among the 12 frequency tests, 10 tests points lie on the off-normal frequency capability curve in NERC PRC-024-3; the other 2 tests points lies within the curve. For all the tests points, the MARS system remains stable, and it provides continuity of operation without tripping during the events. The NERC PRC-024-2 curve was chosen because bulk power system reliability guidelines are applicable to MARS.

Three-phase faults with varied magnitudes and varied duration have been tested for 30 operating conditions. Most of the test cases are on the voltage ride-through time duration curve in NERC PRC-024-3. Only two test points are outside the curve to perform long-duration stress tests. In these tests, fault magnitudes of 0.9 and 1.1, respectively, are considered and both have a fault duration of 10,000 s. Different magnitudes of the fault ride-through tests are achieved by modified the inductance (low-voltage fault) or capacitance (over-voltage fault) of the three-phase fault and varying the location of the fault. For all the tests points, the MARS system remains stable, and it provides continuity of operation without tripping during the events.

These tests showcase compliance to voltage and frequency disturbances found in related reliability recommendations.

3.17.1.2 Harmonics compliance with IEEE 519-2014

The total demand distortion (TDD) of the grid current of the MARS system at Pittsburg was calculated under different operating conditions and was observed to be well below the recommended limits of IEEE 519-2014 (<<2%) [58]. This indicates that the MARS system is in compliance with IEEE 519-2014, and the harmonics injected into the system by the MARS system do not affect the grid system. One of the test results, shown in Figure 56, indicates that the TDD is within the prescribed limits.

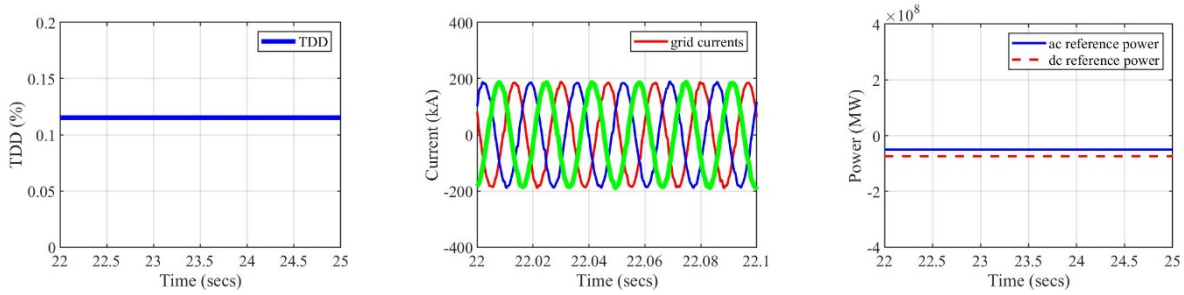

(a) (b) (c)

Figure 56. Harmonics compliance for cHIL test P_{ac} = -50 MW and P_{dc} = -74 MW: (a) TDD for grid currents, (b) instantaneous grid currents, (c) P_{ac} and P_{dc} reference powers.

Milestone M 17.0, "Standards compliance of MARS," has been completed.

4. SIGNIFICANT ACCOMPLISHMENTS AND CONCLUSIONS

One of the significant results obtained in this project is the reduction in costs associated with integrated development through MARS as compared to discrete development of state-of-art existing technologies. The reduced costs are by up to 40% in electrical costs and on the order of 25% in LCOE. The reduced costs provide a good value proposition to integrate PV and ESS through an integrated power electronics solution like MARS. The value proposition can be further extended through identifying the value of optimized power flow through both HVdc and transmission the ac grid at the specific sites chosen. Moreover, the value of reliability benefits provided by MARS through improved coordinated PV and ESS operation at a faster timescale (as opposed to the management of PV and ESS that may happen at a slower timescale) may provide addition value. The MARS technology, as compared to the discrete development, can reduce losses by up to 50%.

The hierarchical control system of MARS proposed for a large-scale integration of PV and ESS to HVdc and transmission the ac grid is unique with its proposed set of control algorithms. It consists of L1, L2, and L3 controllers that have unique sets of control algorithms. For example, in the L1 controller, different voltage and frequency support (grid-forming) algorithms were evaluated that include VSGs, SGs, and MPC-based SGs. In very low SCR conditions, SG and MPC-based SGs are stable but VSGs are not. An EBC, along with a criteria-driven requirement for the EBC, is incorporated in L1 controller to harmonize different sources within MARS while ensuring optimum efficiency of operation. AI-and physics-based bad data and command detection (FDI detection) algorithms are developed in lower and upper layers of L1 controller. The voltage-balancing algorithm is upgraded for MARS (as compared to an HVdc substation) to enhance stability with different sources within MARS. Overall, up to 16% improved frequency response, 100% continuous operation during tested faults, and 100% bad data or FDI detection (if measured data or commands are intruded upon) were observed. Moreover, transient stability is maintained between PV and ESS resources while coordinating the power transfer to HVdc and the transmission ac grid by the proposed hierarchical control system.

To perform the analysis of MARS, advanced EMT simulation algorithms that speed up on the order of tens of thousands and provide greater than 98% accuracy are observed to be valuable. These algorithms, along with pipelining techniques, were utilized in real-time simulation models to ensure high-fidelity dynamic model simulation in real time with a sub-microsecond time step. Without these algorithms, it may have been extremely challenging to perform the analysis completed in this project.

5. BUDGET AND SCHEDULE

Total Budget: $2,500,000 (DOE), $625,000 (cost-share)

Budget Period: 10/01/2018 to 03/31/2022

Modification: Due to delayed subcontracting and changes happening in the management of one of our partners, a 3-month extension was requested and approved in the first year. Toward the end of the project, a 3-month extension was requested to complete the detailed analysis in standards.

6. PATH FORWARD

In this project, the MARS technology as a stand-alone system has been evaluated in depth through HIL testing to showcase the stability of the proposed hierarchical control system. A single module in MARS has been developed to characterize the efficiency of individual modules in MARS and to determine the cost of modules. The next steps upon the completion of the project will be to showcase the utility of MARS technology in different locations in the United States, continue to develop the MARS technology, and develop a laboratory-scale D-MARS technology for field testing.

The next steps for continued research of this technology will be the following:

1. Evaluate technical feasibility to integrate MARS to existing HVdc links as an additional terminal and/or through upgrades to an existing substation. These links are largely based on LCCs.
2. Perform techno-economic feasibility analysis to integrate MARS to multi-terminal dc (MTdc) links with VSCs in future power grids. The MTdc links and HVdc links to integrate renewables are being explored in the Southwest Power Pool (SPP), Midcontinent Independent System Operator (MISO), California Independent System Operator (CAISO), and Electric Reliability Council of Texas (ERCOT).
3. Research and develop protection systems within MARS to differentiate the different internal and external faults and identify the protection algorithms that are needed.
4. Research and develop optimized D-MARS configuration for integration of PVs and ESSs in distribution grid and MVdc links.

Additional aspects of this project could be explored more in detail, such as the EMT simulation algorithms and transient stability (TS) to EMT conversion methods, AI-based cyber-security methods proposed in this project, and sizing methods for energy storage within hybrid plants.

7. INVENTIONS, PATENTS, PUBLICATIONS, AND OTHER RESULTS

Publications

1. S. Debnath, P. R. V. Marthi, Q. Xia, J. Pan, M. Saeedifard, V. N. Vipin, S. Chakraborty, Md Arifujjaman, "Renewable Integration in Hybrid AC/DC Systems Using a Multi-Port Autonomous Reconfigurable Solar Power Plant (MARS)," in IEEE Transactions on Power Systems, vol. 36, no. 1, pp. 603-612, Jan. 2021, doi: 10.1109/TPWRS.2020.3037520.
2. P. R. V. Marthi, S. Debnath, Q. Xia and M. Saeedifard, "Advanced Models and Fast Simulation Algorithms for MARS Plants," 2020 IEEE/PES Transmission and Distribution Conference and Exposition (T&D), 2020, pp. 1-5, doi: 10.1109/TD39804.2020.9299950.
3. Q. Xia, S. Debnath, P. R. V. Marthi, S. Marti and M. Saeedifard, "High-Fidelity Models and Fast EMT Simulation Algorithms for Isolated Multi-port Autonomous Reconfigurable Solar power plant (MARS)," 2021 IEEE 12th International Symposium on Power Electronics for Distributed Generation Systems (PEDG), 2021, pp. 1-7, doi: 10.1109/PEDG51384.2021.9494179.
4. S. Debnath, Q. Xia, M. Saeedifard, and Md Arifujjaman, “Advanced High-Fidelity Lumped EMT Grid Modelling & Comparison”, 2019 Grid of the Future Symposium.
5. Q. Xia, S. Debnath, M. Saeedifard, P. R. V. Marthi and M. Arifujjaman, "Energy Storage Sizing and Operation of an Integrated Utility-Scale PV+ESS Power Plant," 2020 IEEE Power & Energy Society Innovative Smart Grid Technologies Conference (ISGT), 2020, pp. 1-5, doi: 10.1109/ISGT45199.2020.9087636.
6. P. R. V. Marthi, S. Debnath and M. L. Crow, "Synchronverter-based Control of Multi-Port Autonomous Reconfigurable Solar Plants (MARS)," 2020 IEEE Energy Conversion Congress and Exposition (ECCE), 2020, pp. 5019-5026, doi: 10.1109/ECCE44975.2020.9236019.
7. P. R. V Marthi, S. Debnath, Q. Xia and M. L. Crow, "Model Based Predictive Control for Frequency Support in Multi-port Autonomous Reconfigurable Solar Plants," 2021 IEEE Power & Energy Society Innovative Smart Grid Technologies Conference (ISGT), 2021, pp. 1-5, doi: 10.1109/ISGT49243.2021.9372172.
8. Z. Dong, S. Debnath, W. Li, Q. Xia, P. R. V. Marthi and S. Chakraborty, "Real-time Simulation Framework for Hardware-in-the-Loop Testing of Multi-port Autonomous Reconfigurable Solar Power Plant (MARS)," 2021 IEEE Energy Conversion Congress and Exposition (ECCE), 2021, pp. 3160-3167, doi: 10.1109/ECCE47101.2021.9595731.
9. Suman Debnath, Shruti Kulkarni, Catherine Schuman, “Intelligent Prediction of States in Multi-port Autonomous Reconfigurable Solar power plant (MARS)”, 2021 IEEE Energy Conversion Congress and Exposition (ECCE), 2021, pp. 1339-1346, doi: 10.1109/ECCE47101.2021.9595128.
10. S. Yin, S. Debnath, Q. Xia, S. Marti, P. Marthi and M. Saeedifard, "Comparison of Simulation of Dual-Active Bridge in Different Simulators and Using Different Simulation Methods," 2021 IEEE 22nd Workshop on Control and Modelling of Power Electronics (COMPEL), 2021, pp. 1-7, doi: 10.1109/COMPEL52922.2021.9645935.
11. S. Yin, S. Debnath, R. Wojda, P. Marthi and M. Saeedifard, "Impact of the Transformer Magnetizing Inductance on the Performance of the Dual-Active Bridge Converter," 2021 IEEE 22nd Workshop on Control and Modelling of Power Electronics (COMPEL), 2021, pp. 1-7, doi: 10.1109/COMPEL52922.2021.9645978.
12. J. Pan, R. Nuqui, S. Debnath, P. R. V Marthi and Q. Xia, " Virtual Synchronous Generator Control of Multi-port Autonomous Reconfigurable Solar Plants (MARS)”, IEEE PES 2022 T&D Conference and Exposition, April 2022.
13. P. R. V. Marthi, S. Debnath, J. Pan, M. L. Crow, “Discrete and Integrated Solutions for Hybrid PV Plants Without Momentary Cessation in Low SCR and High Penetration PE Grids”, IEEE Kansas Power & Energy Society Conference (KPEC), May 2022.

14. S. Debnath, P. R. V. Marthi, Z. Dong, Q. Xia and S. Chakraborty, "Power Electronic Hardware-in-the-Loop (PE-HIL): Testing Individual Controllers in Large-Scale Power Electronics Systems," *2022 IEEE Energy Conversion Congress and Exposition (ECCE)*, Detroit, MI, USA, 2022, pp. 1-8.

Invention disclosures

The following invention disclosures are filed:

1. “Frequency Response Control of Renewable-plus-storage Power Plant” by Jiuping Pan, Reynaldo Nuqui, Li Qi.
2. “Three-phase continuously varied series reactor” by Rafal Wojda, Suman Debnath.
3. “Stability Intelligence in Hybrid PV Plants (SIP)” by Suman Debnath.
4. “Secure Measurements of HVDC Converter Station” by HyoJong Lee, Jiuping Pan, Reynaldo Nuqui.
5. “Bad Data Detection for Large-Scale PEs” by Suman Debnath, Phani Marthi.
6. “Integrated Control System for Large-Scale PEs” by Suman Debnath, Qianxue Xia, Phani Marthi, Maryam Saeedifard.
7. “Multi-port Autonomous Reconfigurable Solar power plant (MARS)” by Suman Debnath, Phani Marthi, Rafal Wojda.

Patents

The following patents are filed:

1. “Evaluation Platform for Submodules in Multiport Autonomous Reconfigurable Solar (MARS) power plant through Power Electronics Hardware-in-the-Loop” by Shilpa Marti, Suman Debnath, Rafal Wojda.
2. “Multi-port Autonomous Reconfigurable Solar power plant (MARS)” by Suman Debnath, Phani Marthi, Rafal Wojda.
3. “Integrated Control System for Large-Scale PEs” by Suman Debnath, Qianxue Xia, Phani Marthi, Maryam Saeedifard.
4. “Bad Data Detection for Large-Scale PEs” by Suman Debnath, Phani Marthi.

Additionally, 17 conference or seminar presentations have been completed, with some of them being invited talks. Three special sessions and tutorials were conducted at leading power electronics and power systems conferences. An industry advisory board of 35 members from utilities, independent system operators, and original equipment manufacturers (OEMs) was formed. There were 3 doctoral students supported through this project. Suman Debnath and Rafal Wojda progressed to become IEEE senior members during the course of the project.

8. REFERENCES

1. T. Soong and P. W. Lehn, “Internal power flow of a modular multilevel converter with distributed energy resources,” IEEE J. Emerg. Sel. Top. Power Electron. vol. 2, no. 4, pp. 1127–1138, Dec. 2014.

2. M. Schroeder and J. Jaeger, “Advanced energy flow control concept of an MMC for unrestricted operation as a multiport device,” vol. 34, no. 11, pp. 11 496–11 512, Nov. 2019.

3. F. Briz, M. López, A. Zapico, A. Rodríguez and D. Díaz-Reigosa, “Operation and control of MMCs using cells with power transfer capability,” in Proc. IEEE Appl. Power Electron. Conf. Expo., Mar. 2015, pp. 980–987.

4. H. Bayat and A. Yazdani, “A hybrid MMC-based photovoltaic and battery energy storage system,” vol. 6, no. 1, pp. 32–40, Mar. 2019.

5. J. Echeverrıa, S. Kouro, M. Perez, and H. Abu-rub, “Multi-modular cascaded dc-dc converter for hvdc grid connection of large-scale photovoltaic power systems,” in IECON 2013 - 39th Annual Conference of the IEEE Industrial Electronics Society, Nov 2013, pp. 6999–7005.

6. T. S. Basu, S. Maiti, and C. Chakraborty, “A hybrid modular multilevel converter for solar power integration,” in 2016 IEEE 7th Power India International Conference (PIICON), Nov 2016, pp. 1–6.

7. H. Nademi, A. Das, R. Burgos, and L. E. Norum, “A new circuit performance of modular multilevel inverter suitable for photovoltaic conversion plants,” IEEE Journal of Emerging and Selected Topics in Power Electronics, vol. 4, no. 2, pp. 393–404, June 2016.

8. M. Vasiladiotis and A. Rufer, “Analysis and control of modular multilevel converters with integrated battery energy storage,” IEEE Transactions on Power Electronics, vol. 30, no. 1, pp. 163–175, Jan 2015.

9. M. A. Perez, D. Arancibia, S. Kouro, and J. Rodriguez, “Modular multilevel converter with integrated storage for solar photovoltaic applications,” in IECON 2013 - 39th Annual Conference of the IEEE Industrial Electronics Society, Nov 2013, pp. 6993–6998.

10. L. Zhang, Z. Zhang, J. Qin, D. Shi and Z. Wang, "Design and Performance Evaluation of the Modular Multilevel Converter (MMC)-based Grid-tied PV-Battery Conversion System," *IEEE Energy Conversion Congress and Exposition (ECCE)*, Portland, OR, 2018, pp. 2649-2654.

11. S. Rivera, B. Wu, R. Lizana, S. Kouro, M. Perez and J. Rodriguez, "Modular multilevel converter for large-scale multistring photovoltaic energy conversion system," *2013 IEEE Energy Conversion Congress and Exposition*, 2013, pp. 1941-1946.

12. F. Rong, X. Gong and S. Huang, "A Novel Grid-Connected PV System Based on MMC to Get the Maximum Power Under Partial Shading Conditions," in *IEEE Transactions on Power Electronics*, vol. 32, no. 6, pp. 4320-4333, June 2017

13. H. Bayat and A. Yazdani, "A Power Mismatch Elimination Strategy for an MMC-Based Photovoltaic System," in *IEEE Transactions on Energy Conversion*, vol. 33, no. 3, pp. 1519-1528, Sept. 2018.

14. H. Bayat and A. Yazdani, "A Hybrid MMC-Based Photovoltaic and Battery Energy Storage System," in *IEEE Power and Energy Technology Systems Journal*, vol. 6, no. 1, pp. 32-40, March 2019.

15. X. Pan, J. Gong, S. Pan and X. Zha, "Circulating Current Analysis and Power Mismatch Elimination Strategy for an MMC-Based Photovoltaic System," *2020 IEEE Energy Conversion Congress and Exposition (ECCE)*, 2020, pp. 105-109.

16. T. Soong and P. W. Lehn, "Assessment of Fault Tolerance in Modular Multilevel Converters With Integrated Energy Storage," in *IEEE Transactions on Power Electronics*, vol. 31, no. 6, pp. 4085-4095, June 2016.

17. N. Li, F. Gao, T. Hao, Z. Ma and C. Zhang, "SOH Balancing Control Method for the MMC Battery Energy Storage System," in *IEEE Transactions on Industrial Electronics*, vol. 65, no. 8, pp. 6581-6591, Aug. 2018.

18. A. Hillers and J. Biela, "Fault-Tolerant Operation of The Modular Multilevel Converter in an Energy Storage System Based on Split Batteries," *2014 16th European Conference on Power Electronics and Applications*, 2014, pp. 1-8.

19. G. Liang *et al*., "Analytical Derivation of Intersubmodule Active Power Disparity Limits in Modular Multilevel Converter-Based Battery Energy Storage Systems," in *IEEE Transactions on Power Electronics*, vol. 36, no. 3, pp. 2864-2874, March 2021.

20. D. I. Doukas, K. Papastergiou, P. Bakas and A. Marinopoulos, "Energy storage sizing for large scale PV power plants base-load operation - comparative study & results," 38th IEEE Photovoltaic Specialists Conference, Austin, TX, 2012, pp. 000570-000574.

21. Y. Yang, Q. Ye, L. J. Tung, M. Greenleaf and H. Li, "Integrated Size and Energy Management Design of Battery Storage to Enhance Grid Integration of Large-Scale PV Power Plants," in *IEEE Transactions on Industrial Electronics*, vol. 65, no. 1, pp. 394-402, Jan. 2018.

22. C. Venu, Y. Riffonneau, S. Bacha and Y. Baghzouz, "Battery Storage System sizing in distribution feeders with distributed photovoltaic systems," *2009 IEEE Bucharest PowerTech*, Bucharest, 2009, pp. 1-5.

23. R. Yu, J. Kleissl, and S. Martinez, "Storage size determination for gridconnected photovoltaic systems," *IEEE Trans. Sustain. Energy*, vol. 4, no. 1, pp. 68–81, Jan. 2013.

24. B. Verhelst, C. Debruyne, J. Vanalme, J. Desmet, J. Capelle, and L. Vandevelde, "Economic evaluation of the influence of overvoltages and the integration of small storage capacity in residential PV-installations," in Proc. *2nd IEEE PES Int. Conf. Exhib. Innov. Smart Grid* Technol., 2011, pp. 1–6.

25. A. Oudalov, R. Cherkaoui, and A. Beguin, "Sizing and optimal operation of battery energy storage system for peak shaving application," in Proc. *IEEE Lausanne Power Tech*, Jul. 2007, pp. 621–625.

26. Y. Yang, H. Li, A. Aichhorn, J. Zheng, and M. Greenleaf, "Sizing strategy of distributed battery storage system with high penetration of photovoltaic for voltage regulation and peak load shaving," *IEEE Trans. Smart Grid*, vol. 5, no. 2, pp. 982–991, Mar. 2014.

27. H. Beltran, E. Bilbao, E. Belenguer, I. Etxeberria-Otadui and P. Rodriguez, "Evaluation of Storage Energy Requirements for Constant Production in PV Power Plants," in *IEEE Transactions on Industrial Electronics*, vol. 60, no. 3, pp. 1225-1234, March 2013.

28. ecdms.energy.ca.gov, 'Electricity Consumption by County', [Online]. Available: https://ecdms.energy.ca.gov/elecbycounty.aspx

29. us-places.com, 'Louisiana population by Parish – total residents', [Online]. Available: https://us-places.com/Louisiana/population-by-Parish.htm

30. us-places.com, 'Arkansas population by County – total residents', [Online]. Available:https://us-places.com/Arkansas/population-by-County.htm

31. us-places.com, 'Mississippi population by County – total residents', [Online]. Available: https://us-places.com/Mississippi/population-by-County.htm

32. us-places.com, 'Georgia population by County – total residents', [Online]. Available: https://us-places.com/Georgia/population-by-County.htm

33. us-places.com, 'Alabama population by County – total residents', [Online]. Available: https://us-places.com/Alabama/population-by-County.htm

34. us-places.com, 'Texas population by County – total residents', [Online]. Available: https://us-places.com/Texas/population-by-County.htm

35. nrel.gov, 'U.S. State Solar Resource Maps', [Online]. Available: https://www.nrel.gov/gis/solar.html

36. pnnl.gov, 'Models and methods for assessing the value of HVdc and MVdc technologies in modern power grids', Annual report, July 2017. [Online]. Available: https://www.pnnl.gov/main/publications/external/technical_reports/PNNL-26640.pdf

37. transbaycable.com, 'Operations', [Online]. Available: http://www.transbaycable.com/operations.html

38. new.abb.com, 'Pacific Intertie', [Online], Available: https://new.abb.com/systems/hvdc/references/pacific-intertie

39. ruskpanolatransmissionproject.com, 'ABOUT THE RUSK-PANOLA TRANSMISSION PROJECT', [Online]. Available: https://ruskpanolatransmissionproject.com/about-the-project/

40. southerncrosstransmission.com, 'The Southern Cross Transmission Project', [Online]. Available: http://southerncrosstransmission.com/

41. transwestexpress.net, 'By the numbers', [Online]. Available: http://www.transwestexpress.net/index.shtml

42. energy.gov, 'Plains & Eastern Clean Line Transmission Project', [Online]. Available: https://www.energy.gov/nepa/eis-0486-plains-eastern-clean-line-transmission-project

43. pvwatts.nrel.gov, 'PVWatts Calculator', [Online]. Available: https://pvwatts.nrel.gov/pvwatts.php

44. sce.com, 'The Clean Power and Electrification Pathway', 2017. [Online]. Available: https://www.edison.com/content/dam/eix/documents/our-perspective/g17-pathway-to-2030-white-paper.pdf

45. S. Debnath and J. Sun, "Fidelity Requirements with Fast Transients from VSC-HVdc," IECON 2018 - 44th Annual Conference of the IEEE Industrial Electronics Society, Washington, DC, 2018, pp. 6007-6014.

46. YV Makarov, MA Elizondo, JG O'Brien, Q Huang, H Kirkham, Z Huang, M Chinthavali, S Debnath, N Mohan, W Hess, D Duebner, D Orser, H Brown, D Osborn, J Feltes, DK Chandrashekhara, W Zhu, "Models and methods for assessing the value of HVDC and MVDC technologies in modern power grids," Technical Report, PNNL-26640, Project GM 0074, Grid Modernization Laboratory Consortium, U.S. Department of Energy, July 2017.

47. S. Debnath, Q. Xia, M. Saeedifard, and Md Arifujjaman, "Advanced High-Fidelity Lumped EMT Grid Modelling & Comparison", 2019 Grid of the Future Symposium.

48. S. Debnath, P. R.V. Marthi, Q.Xia, et al., "Renewable Integration in Hybrid AC/DC Systems Using a Multi-Port Autonomous Reconfigurable Solar Power Plant (MARS)," in IEEE Transactions on Power Systems, vol. 36, no. 1, pp. 603-612, Jan. 2021, doi: 10.1109/TPWRS.2020.3037520.

49. P. R. V. Marthi, S. Debnath, Q. Xia and M. Saeedifard, "Advanced Models and Fast Simulation Algorithms for MARS Plants," 2020 IEEE/PES Transmission and Distribution Conference and Exposition (T&D), 2020, pp. 1-5, doi: 10.1109/TD39804.2020.9299950.

50. Q. Xia, S. Debnath, P. R. V. Marthi, S. Marti and M. Saeedifard, "High-Fidelity Models and Fast EMT Simulation Algorithms for Isolated Multi-port Autonomous Reconfigurable Solar power plant (MARS)," 2021 IEEE 12th International Symposium on Power Electronics for Distributed Generation Systems (PEDG), 2021, pp. 1-7, doi: 10.1109/PEDG51384.2021.9494179.

51. https://info.ornl.gov/sites/publications/Files/Pub124769.pdf

52. http://www.ewh.ieee.org/r6/san_francisco/pes/pes_pdf/Transbay_Cable.pdf

53. R. Fu, et al, "2018 U.S. Utility-Scale Photovoltaics-Plus-Energy Storage System Costs Benchmark", NREL Report, November 2018.

54. EIA Report, "Levelized Cost and Levelized Avoided Cost of New Generation Resources in the Annual Energy Outlook 2019", February 2019.

55. EIA Report, "Assessing HVDC Transmission for Impacts of Non-Dispatchable Generation", June 2018.

56. T. Hennig, "Review of Investment Model Cost Parameters for VSC HVDC Transmission Infrastructure", Electric Power Systems Research, August 2017.

57. NERC, "Frequency and Voltage Protection Settings for Generating Resources," PRC-024-3, July 2020. url: https://www.nerc.com/pa/Stand/Reliability%20Standards/PRC-024-3.pdf

58. IEEE, "IEEE Standard for Interconnection and Interoperability of Distributed Energy Resources with Associated Electric Power Systems Interfaces," IEEE Std 1547-2018 (Revision of IEEE Std 1547-2003), 6 April 2018.

APPENDIX A. DESIGN AND DEVELOPMENT OF MARS SOFTWARE AND SIMULATION MODELS

APPENDIX A. DESIGN AND DEVELOPMENT OF MARS SOFTWARE AND HARDWARE

A.1 3.2 DESIGN AND DEVELOP REDUCED-ORDER MODEL OF MARS

A.1.1 3.2.1 Design MARS circuit based on the ESS and PV plant size

The parameters of the MARS circuit at Victorville, California, is tabulated in Table A.1.

Table A.1. Ratings for MARS

Location	Victorville (CA)
System Rating (MW)	1000.0
dc Voltage Rating (kV)	±525.0
ac Voltage Rating (kV)	500.0
P_{PV} Rating (MW)	1000.0
P_{ESS} Rating (MW)	389.8
E_{ESS} Rating (MWh)	1,232.3

A.2 3.3 DEVELOP SIMULATION ALGORITHMS AND HIGH-FIDELITY MODELS OF MARS

A.2.1 3.3.1 Develop high-fidelity models of MARS

Arm Current Dynamics

The dynamics of the arm currents in the MARS system are given by the following equations

$$(L_{\mathrm{o}} + L_{\mathrm{s}})\frac{\mathrm{d}i_{\mathrm{p},j}}{\mathrm{d}t} - L_{\mathrm{s}}\frac{\mathrm{d}i_{\mathrm{n},j}}{\mathrm{d}t} = -(R_{\mathrm{o}} + R_{\mathrm{s}})\, i_{\mathrm{p},j} + R_{\mathrm{s}}\, i_{\mathrm{n},j} + \frac{V_{\mathrm{dc}}}{2} - v_j - v_{\mathrm{cm}} - v_{\mathrm{p},j}\,, \forall j \in (a,b,c) \quad \text{(A.1a)}$$

$$(L_{\mathrm{o}} + L_{\mathrm{s}})\frac{\mathrm{d}i_{\mathrm{n},j}}{\mathrm{d}t} - L_{\mathrm{s}}\frac{\mathrm{d}i_{\mathrm{p},j}}{\mathrm{d}t} = -(R_{\mathrm{o}} + R_{\mathrm{s}})\, i_{\mathrm{n},j} + R_{\mathrm{s}}\, i_{\mathrm{p},j} + \frac{V_{\mathrm{dc}}}{2} + v_j + v_{\mathrm{cm}} - v_{\mathrm{n},j}\,, \forall j \in (a,b,c) \quad \text{(A.1b)}$$

$$v_{\mathrm{y},j} = \sum_{\mathrm{l}=1}^{\mathrm{N_{norm}}} v_{\mathrm{smnorm,y,l},j} + \sum_{\mathrm{l}=\mathrm{N_{norm}}+1}^{\mathrm{N_{pv}}} v_{\mathrm{smpv,y,l},j} + \sum_{\mathrm{l}=\mathrm{N_{pv}}+1}^{\mathrm{N_{ess}}} v_{\mathrm{smess,y,l},j}, \forall\, \mathrm{y} \in (\mathrm{p,n}),\, \forall\, j \in (a,b,c) \quad \text{(A.1c)}$$

$$\sum_{\mathrm{l}=1}^{\mathrm{N_{norm}}} v_{\mathrm{smnorm,y,l},j} = \sum_{\mathrm{l}=1}^{\mathrm{N_{norm}}} \left[S_{\mathrm{y,l},j,1} v_{\mathrm{cy,l},j} + \left\{(1 - S_{\mathrm{y,l},j,1})(1 - S_{\mathrm{y,l},j,2}) v_{\mathrm{cy,l},j}\right\} \mathrm{sgn}(i_{\mathrm{y},j})\right],$$

$$\forall\, \mathrm{y} \in (\mathrm{p,n}),\, \forall\, j \in (a,b,c) \quad \text{(A.1d)}$$

$$\sum_{\mathrm{l}=\mathrm{N_{norm}}+1}^{\mathrm{N_{pv}}} v_{\mathrm{smpv,y,l},j} = \sum_{\mathrm{l}=\mathrm{N_{norm}}+1}^{\mathrm{N_{pv}}} \left[S_{\mathrm{y,l},j,1} v_{\mathrm{cy,l},j} + \left\{(1 - S_{\mathrm{y,l},j,1})(1 - S_{\mathrm{y,l},j,2}) v_{\mathrm{cy,l},j}\right\} \mathrm{sgn}(i_{\mathrm{y},j})\right],$$

$$\forall\, \mathrm{y} \in (\mathrm{p,n}),\, \forall\, j \in (a,b,c) \quad \text{(A.1e)}$$

$$\sum_{l=N_{pv}+1}^{N_{ess}} v_{smess,y,l,j} = \sum_{l=N_{pv}+1}^{N_{ess}} \left[S_{y,l,j,1} v_{cy,l,j} + \{(1 - S_{y,l,j,1})(1 - S_{y,l,j,2}) v_{cy,l,j}\} \text{sgn}(i_{y,j})\right],$$

$$\forall\, y \in (p,n), \forall\, j \in (a,b,c) \tag{A.1f}$$

The dynamics of the normal SM capacitor voltages in MARS are given by

$$C_{SM} \frac{dv_{cy,i,j}}{dt} = -\frac{v_{cyi,j}}{R_p} + S_{y,i,j,3} i_{y,j} + (1 - S_{y,i,j,1})(1 - S_{y,i,j,2}) i_{y,j} \text{sgn}(i_{y,j}) \tag{A.1g}$$

A.2.2 3.3.4 Test and validate the developed high-fidelity models

The dc link currents from simulation of different use cases of MARS are shown in Figure A.1 that include the different operating modes of MARS. In all these figures, it may be observed that the developed high-fidelity EMT model of MARS is extremely accurate when compared to the baseline model of MARS.

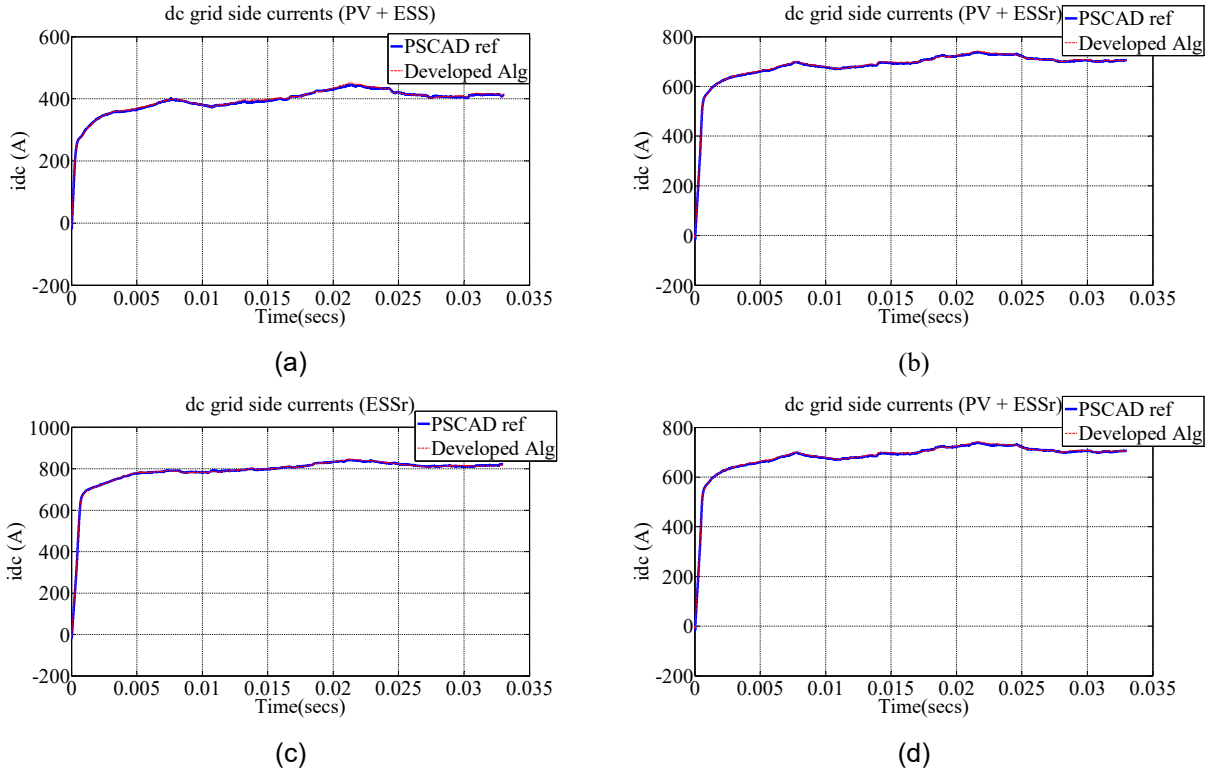

Figure A.1. dc bus current in MARS Pittsburg: (a) for PV and ESS full rating (with both PV and ESS power generation) (b) for PV and ESSr full rating (with PV power generation and ESS charging), (c) for only ESS reverse flow (with only ESS being charged), (d) for only PV (with only PV generation).

A.3 3.4 DESIGN AND DEVELOP OFFLINE CONTROL ALGORITHMS IN MARS

A.3.1 3.4.2 Develop SG (virtual) algorithms to support frequency and voltage

To provide fast primary frequency response and voltage support during ac-side disturbances, different control algorithms in L1 control are evaluated for different use cases and scenarios in this project. In addition to VSG control algorithm the different control algorithms developed include (a) SG-based

control algorithm; and (b) model predictive control (MPC)-based SG control algorithm. The VSG control algorithm is mostly beneficial for providing support during frequency disturbances and voltage disturbances caused during balanced and unbalanced transmission faults in the case when MARS is connected to stronger ac grid (with SCR greater than 2). With the help of VSG-based control algorithms up to ***~16% improvement*** is observed in the frequency nadir of the system. In the case of SG-based and MPC-based SG algorithms, the stable frequency response for extremely low SCR scenarios (of less than 2 and higher than 0.5) was possible with up to ~8% improvement observed. In very low SCR cases, VSG-based control algorithms are unstable.

A.3.2 3.4.3 Develop harmonized source control methods

The lowest level controllers (L3) are shown in Figure A.2 and Figure A.3. The former is the controller for ESS, and the latter is the controller for PV systems.

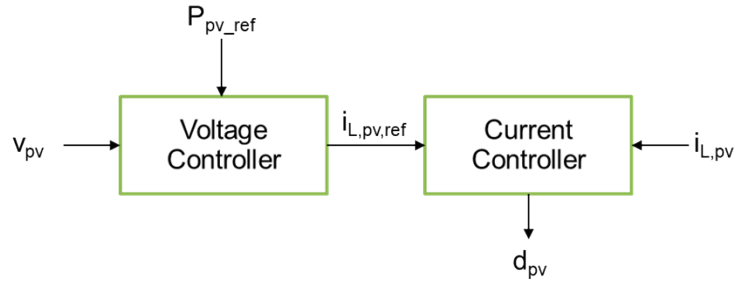

Figure A.2. L3 ESS controller.

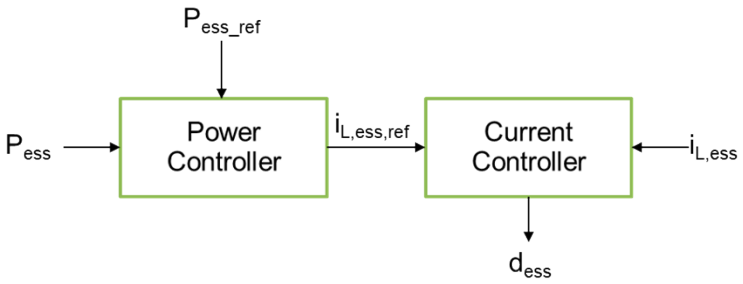

Figure A.3. L3 PV controller.

In Figure A.2, the bi-directional dc-dc converter control for the ESS SM is provided. The dc-dc converter is controlled by employing an outer PI control to control the power required by the batteries and an inner PI control to control the inductor current. In Figure A.3, the dc-dc converter control for the PV SM is provided. The dc-dc converter is controlled by employing an outer voltage controller and an inner current controller.

A.4 3.11 DESIGN AND DEVELOP CYBER HARDWARE IN LOWER-LEVEL CONTROLLERS AND IMPLEMENT CYBER-SECURE SOLUTIONS IN HIGHER-LEVEL CONTROLLER

A.4.1 3.11.1 Design cyber protection system

In addition to the secure power command functionality introduced in the high-level L1 controller, the secure MARS measurement functionality is introduced. The secure MARS measurement (secure MARS

MEAS) is a detection algorithm that identifies the manipulated voltage measurement (that is used in the VSG control). The method can block and mitigate unwarranted emergency power control such as frequency response or dynamic voltage support functions in the VSG controller when it detects the faulty measurements.

The secure MARS MEAS has two features: one measurement consistency check and two measurements consistency check. They are described more in detail below.

1. *One measurement consistency check:* This detection function checks the consistency of the frequency derived from each phase of a three-phase signal with other two phases. This function is useful to detect single-phase manipulated measurement.
2. *Two measurements consistency check:* This detection function checks the consistency of the frequency derived from two independent measurements like voltages measured at different locations. This function can detect single, two, or three-phase manipulated measurement.